

**Best  
Available  
Copy**

AD-A007 733

DIFFERENTIAL SEA ICE DRIFT

W. D. Hibler, III, et al

Cold Regions Research and Engineering  
Laboratory

Prepared for:

National Science Foundation  
Advanced Research Projects Agency

March 1975

DISTRIBUTED BY:

**NTIS**

National Technical Information Service  
U. S. DEPARTMENT OF COMMERCE

ii a

The findings in this report are not to be construed as an official Department of the Army position unless so designated by other authorized documents.

ACCESSION for		
NTIS	White Section	<input checked="checked" type="checkbox"/>
P 3	Def. Section	<input type="checkbox"/>
UNCLASSIFIED		<input type="checkbox"/>
JCS/AFM/...		
BY		
DISTRIBUTION/AVAILABILITY CODES		
DISC.	AVAIL.	and/or SPECIAL
A		

Unclassified

SECURITY CLASSIFICATION OF THIS PAGE (When Data Entered)

REPORT DOCUMENTATION PAGE		READ INSTRUCTIONS BEFORE COMPLETING FORM	
1. REPORT NUMBER Research Report 329	2. GOVT ACCESSION NO.	3. RECIPIENT'S CATALOG NUMBER AD-A007 733	
4. TITLE (and Subtitle) DIFFERENTIAL SEA ICE DRIFT		5. TYPE OF REPORT & PERIOD COVERED	
		6. PERFORMING ORG. REPORT NUMBER	
7. AUTHOR(s) W.D. Hibler III, W.F. Weeks, A. Kovacs and S.F. Ackley		8. CONTRACT OR GRANT NUMBER(s) NSF Grants AG 344 and AG 492 ARPA Order 1615	
9. PERFORMING ORGANIZATION NAME AND ADDRESS U.S. Army Cold Regions Research and Engineering Laboratory Hanover, N.H. 03755		10. PROGRAM ELEMENT, PROJECT, TASK AREA & WORK UNIT NUMBERS	
11. CONTROLLING OFFICE NAME AND ADDRESS National Science Foundation, Washington, D.C. Advanced Research Projects Agency, Arlington, Va.		12. REPORT DATE March 1975	
		13. NUMBER OF PAGES 44	
14. MONITORING AGENCY NAME & ADDRESS (if different from Controlling Office)		15. SECURITY CLASS. (of this report) Unclassified	
		15a. DECLASSIFICATION/DOWNGRADING SCHEDULE	
16. DISTRIBUTION STATEMENT (of this Report)  Approved for public release; distribution unlimited.			
17. DISTRIBUTION STATEMENT (of the abstract entered in Block 20, if different from Report)			
18. SUPPLEMENTARY NOTES  Reproduced by NATIONAL TECHNICAL INFORMATION SERVICE U.S. Department of Commerce Springfield, VA 22151  PRICES SUBJECT TO CHANGE			
19. KEY WORDS (Continue on reverse side if necessary and identify by block number)			
Continuum motion	Ice physics	Pack ice	Strain measurements
Cross spectral analysis	Inhomogeneity variation	Pack ice rotation	Velocity fluctuations
Divergence rates	Linear drift theory	Sea ice deformation	Viscous sea ice models
Ekman layer theory	Linear least squares theory	Sea ice drift	Wind driven ice drift
Ice mechanics	Memory effects	Spectral analysis	
20. ABSTRACT (Continue on reverse side if necessary and identify by block number)			
<p>Measurements of mesoscale sea ice deformation over a region approximately 20 km in diameter were made over a five-week period in the spring of 1972 at the main AIDJEX camp in the Beaufort Sea. They have been analyzed to determine nonlinearities in the ice velocity field (due to the discrete small-scale nature of the ice pack), as well as a continuum mode of deformation represented by a least squares strain rate tensor and vorticity. The deformation rate time series between Julian day 88 and 113 exhibited net areal changes as large as 3% and deformation rates up to 0.16% per hour. In the principal axis coordinate system, the strain rate typically exhibited a much larger compression (or extension) along one axis than along the other. Persistent cycles at ~ 12-hour wavelengths were observed in the divergence rate.</p>			

DD FORM 1 JAN 73 1473

EDITION OF 1 NOV 65 IS OBSOLETE

Unclassified

SECURITY CLASSIFICATION OF THIS PAGE (When Data Entered)

20.

A comparison of the average residual error with the average strain rate magnitude indicated that strains measured on a scale of 10 km or greater can serve as a valid measure of the continuum motion of the sea ice. This conclusion is also substantiated by a comparison between the mesoscale deformation, and macroscale deformation measured over a  $\sim 100$ -km-diameter region. Vorticity calculations indicate that at low temporal frequencies ( $< 0.04 \text{ hr}^{-1}$ ) the whole mesoscale array rotates essentially as an entity and consequently the low frequency vorticity can accurately be estimated from the rotation of a single floe. (Part I)

A comparison of mesoscale strain measurements with the atmospheric pressure field and the wind velocity field indicated that the ice divergence rate and vorticity followed the local pressure and wind divergence with significant correlation. For low atmospheric pressures and converging winds, the divergence rate was negative with the vorticity being counterclockwise. The inverse behavior was observed for high pressures and diverging winds. This behavior agreed with predictions based upon the infinite boundary solution of a linearized drift theory in the absence of gradient current effects and using the constitutive law proposed by Glen for pack ice. The best least squares values of the constitutive law parameters  $\eta$  and  $\zeta$  were found to be given by  $\sim 10^{12} \text{ kg sec}^{-1}$ . Using typical divergence rates, these values yielded compressive stresses of the magnitude of  $10^5 \text{ N m}^{-1}$  which are similar to values suggested by the Parmerter and Coon ridge model. In general, the infinite boundary solution of the linear drift equation indicates that in a low pressure region that is reasonably localized in space, the ice would be expected to converge for high compactness (winter) and diverge for low compactness (summer). Calculations were also carried out using a more general linear viscoelastic constitutive law that includes memory effects and that includes a generalized Hooke's law as well as the Glen law as special cases. A best fit of this more general calculation with strain measurements indicates, overall, a better agreement with viscous behavior than with elastic behavior, with the frequency behavior of the estimated "viscosities" similar to the Glen law behavior at temporal frequencies less than  $\sim 0.01 \text{ hr}^{-1}$ . (Part II)

## PREFACE

This report was prepared in two parts. Part I was prepared by Dr. W.D. Hibler III, Research Solid State Physicist, Dr. W.F. Weeks, Glaciologist, A. Kovacs, Research Civil Engineer, and S.F. Ackley, Research Solid State Physicist. Part II was prepared by Dr. W.D. Hibler III. Dr. Hibler, Dr. Weeks and S.F. Ackley are members of the Snow and Ice Branch, Research Division, and A. Kovacs is a member of the Foundations and Materials Research Branch, Experimental Engineering Division, U.S. Army Cold Regions Research and Engineering Laboratory (USA CRREL).

This study was funded by the National Science Foundation under NSF Grants AG 344 and AG 492 and by the Advanced Research Projects Agency under ARPA Order 1615.

This report was technically reviewed by S.J. Mock and Dr. G.D. Ashton of USA CRREL.

The authors of Part I would like to express thanks to Dr. W.J. Campbell for interesting them in developing a mesoscale strain program and for his valuable assistance during the field study. Thanks are also due to J. Taylor and G.F.N. Cox for their assistance in manning the laser array. A. Thorndike kindly provided processed macroscale drift and deformation data and, together with A. Gill, provided information on the rotation of the base camp.

Thanks are also expressed to Dr. J. Nye for his comments on a draft version of the report and to A. Johnson for editing the final version. Finally, appreciation is expressed to the staff of the Arctic Ice Dynamics Joint Experiment (AIDJEX) project for support which made this program possible.

Dr. Hibler, the author of Part II, would like to thank D.A. Rothrock for helpful discussions on linear drift theories and for continuing constructive criticism of earlier calculations that motivated this research. Discussions with W.F. Weeks and S.F. Ackley, and comments by J.F. Nye on constitutive laws, were also of considerable aid. A. Thorndike and P. Martin kindly provided remote buoy pressure data.

## CONTENTS

	Page
General Introduction	1
Part I. Spatial and temporal variations in sea ice deformation	2
Introduction	2
Approach	2
Site location and data collection procedures	4
Data analysis	5
Strain results	9
Comparison of mesoscale deformation with macroscale deformation	14
Nature of the ice pack rotation	17
Conclusion	19
Literature cited	19
Part II. Comparison of mesoscale strain measurements with linear drift theory predictions	21
Introduction	21
List of symbols	21
Linear drift equations	22
Ice drift solutions	23
Comparison of theory with mesoscale measurements	27
A more general linear constitutive law	31
Conclusions	33
Literature cited	34
Appendix. Relative magnitudes of differential drift forces	37
Abstract	39

## ILLUSTRATIONS

### Part I

Figure	
1. Schematic diagram of the mesoscale strain array together with active leads and ridging zones	3
2. Typical results of the interpolation and smoothing process used to generate equispaced values for the strain analysis	5
3. Least squares divergence rate and accompanying inhomogeneity error, and maximum shear rate and inhomogeneity error	10
4. Principal axis components of the least squares strain rate tensor and inhomogeneity errors	10
5. Comparison of mesoscale divergence rate, north-south strain rate, east-west strain rate, shear rate, least squares residual fluctuation error, east-west velocity of the camp, north-south velocity of the camp, and speed of the camp	12
6. Comparison of net divergences of overlapping triangles	13
7. Comparison of mesoscale and macroscale divergence rates, vorticities, and maximum shear rates	16

Figure	Page
8. Power spectra of mesoscale divergence rate, and shear rate; and macro-scale divergence rate, shear rate and vorticity	17
9. Camp rotation rate and mesoscale vorticity	18
10. Comparison of east-west shear rate and vorticity	18

## Part II

Figure	
1. Wave number space response functions for the divergence rate and vorticity of the ice pack for different values of $\eta$ and $\zeta$	26
2. Comparison of experimental time series calculated from AIDJEX 1972 data	28
3. Spectra of atmospheric pressure and mesoscale ice divergence rate at the main AIDJEX 1972 camp	29
4. Coherence spectra and phase angles between a) vorticity and atmospheric pressure and b) divergence rate and atmospheric pressure	33
5. Frequency dependence of the generalized bulk and shear viscosity amplitudes	33

## TABLES

### Part I

Table	
I. Strain line combinations used in this paper	9
II. Root-mean-square strain rates, strain rate variation errors and experimental errors for combined array	11
III. Root-mean-square strain rates, residual errors, and central point velocities	14
IV. Meso- and macroscale root-mean-square deformation rates and correlation coefficients	15

### Part II

Table	
I. Correlation coefficient matrix between time series	28
II. Estimates of $\eta$ and $\zeta$	30



## DIFFERENTIAL SEA ICE DRIFT

### GENERAL INTRODUCTION

The development of an accurate predictive model for the motion and deformation of arctic pack ice is believed by most engineers and scientists concerned with arctic research and development to be of prime importance both for practical operational purposes and for climatological considerations. In order to develop such a model, it was realized in the latter part of the 1960's that simultaneous measurements of the drift of several different points on the ice cover, together with appropriate meteorological and oceanographic measurements, were required (Untersteiner and Hunkins 1969\*). The basic reason for this is that accurate drift calculations depend upon understanding the magnitude of forces caused by the pack ice interacting with itself. To obtain an understanding of these forces, it is necessary to measure the way a given area of ice deforms or "strains" in time. Such deformation is a result of differences between ice velocities at different locations and hence in general can be referred to as *differential drift*.

One of the basic experimental aspects of AIDJEX (Arctic Ice Dynamics Joint Experiment (see, for example, Maykut et al. 1972†), has been to measure such differential drift as well as absolute drift. In the springs of 1971 and 1972, pilot studies were conducted, one purposes of which was to determine the optimal way of sampling the ice velocity field in order to measure the differential drift in an adequate manner for determining a reasonable continuum constitutive law describing pack ice. During these pilot studies CRREL carried out, among other studies, a mesoscale strain program. In this program the ice velocity field was sampled in a region approximately 25 km in diameter. The measurements of the 1971 experiment were sparsely spaced in both time and space but did yield valuable quantitative information (Hibler et al. 1973\*\*) on mesoscale strain not theretofore available. In the 1972 experiment a much more extensive set of measurements – dense in both time and space – was obtained which made possible the calculation of various deformation time series at 3-hour intervals over a period of more than 30 days. The results allowed a detailed study to be made of the nature of the ice velocity field. Also, using available meteorological data, the results were compared with theoretical ice drift models with good success.

This report, divided into two parts, describes the analysis of the 1972 results. Part I examines the results with a view toward understanding of the nature of the ice velocity field and determining the minimum scale on which the pack ice may be viewed as a continuum. Part II represents the formulation of an analytic solution of a linear drift model which includes ocean, air and Coriolis forces and models the ice as a viscoelastic medium. The predicted results of this calculation (based on meteorological variables) are compared with observed differential drift measurements with good agreement and a number of conclusions regarding ice drift calculations using a linear model are drawn.

\* Untersteiner, N. and K.L. Hunkins (1969) Arctic ice deformation joint experiment, Final Report. University of Washington, Office of Naval Research, Contract N00014-67-A-0103-0004, 39 p.

† Maykut, G.A., A.S. Thorndike and N. Untersteiner (1972) AIDJEX scientific plan. University of Washington, Division of Marine Resources, AIDJEX Bulletin no. 15, 67 p.

\*\* Hibler, W.D. III, W.F. Weeks, S. Ackley, A. Kovacs and W.J. Campbell (1973) Mesoscale strain measurements on the Beaufort Sea pack ice (AIDJEX 1971). *Journal of Glaciology*, vol. 12, no. 65, p. 187-206.

## PART I. SPATIAL AND TEMPORAL VARIATIONS IN SEA ICE DEFORMATION

by

W.D. Hibler III, W.F. Weeks, A. Kovacs and S.F. Ackley

### Introduction

One of the primary goals of the Arctic Ice Dynamics Joint Experiment (AIDJEX) is an improved understanding of the drift of pack ice. To this end accurate field observations of the deformation of different types of pack ice performed on a variety of time and space scales are urgently needed. To partially satisfy this need a series of detailed mesoscale strain measurements were made at approximately 3-hour intervals over a 30-day period in the spring of 1972 in the Beaufort Sea. These measurements are particularly useful, since in earlier studies of sea ice deformation – as reviewed, for example, by Hibler et al. (1973a) – there were usually large and random time intervals between observations, making the computation of accurate time series impossible. Also, and perhaps even more important, these earlier studies included no detailed investigation of the nonlinear variations in the ice velocity field that result from inhomogeneous spatial variations or fluctuations in the deformation of the ice.

Therefore, the analysis described here was undertaken with three primary goals in mind: first, to provide a detailed time series of the least squares strain rate tensor and vorticity (complete with "error bars" due to the nonlinearity of the ice velocity field) over the 25-day period, Julian day 88-113 (28 Mar-22 Apr), 1972; second, to study the magnitude and nature of the nonlinear velocity fluctuations; and third, to compare deformation measures from different scales to determine coherent modes of deformation in different sized arrays as well as scaling effects. These results can then be compared with predictions from theoretical drift calculations and with data collected on the remote sensing overflights. Besides providing insight into the nature of pack ice dynamics, such comparisons and information on inhomogeneities in the ice velocity field are helpful in designing future strain arrays.

### Approach

As a framework in which to view our analysis, it is useful to think of the pack as a large number of irregular ice floes packed closely together, with the compactness varying with season. In the summer, when the compactness is low, the individual ice floes can readily be identified and the pack looks like a two-dimensional granular medium. In the winter, when the compactness is near one, the individual floes can no longer be clearly identified and the ice is crisscrossed by a number of irregular leads. A typical example of the pack ice structure in winter is given in Figure 1, which shows a schematic diagram of active leads and ridging zones in the mesoscale strain array for one instant of time.

Using such a conceptual model of pack ice, the velocity of any point in the pack can be viewed as consisting of a continuum velocity component (varying over lengths commensurate with the scale of meteorological variations) plus a fluctuation component due to the discrete small-scale nature of the pack ice. Such a partition of the velocity field is similar to that which can be made for a fluid where the motion of each molecule has a continuum component plus a fluctuation component. In the

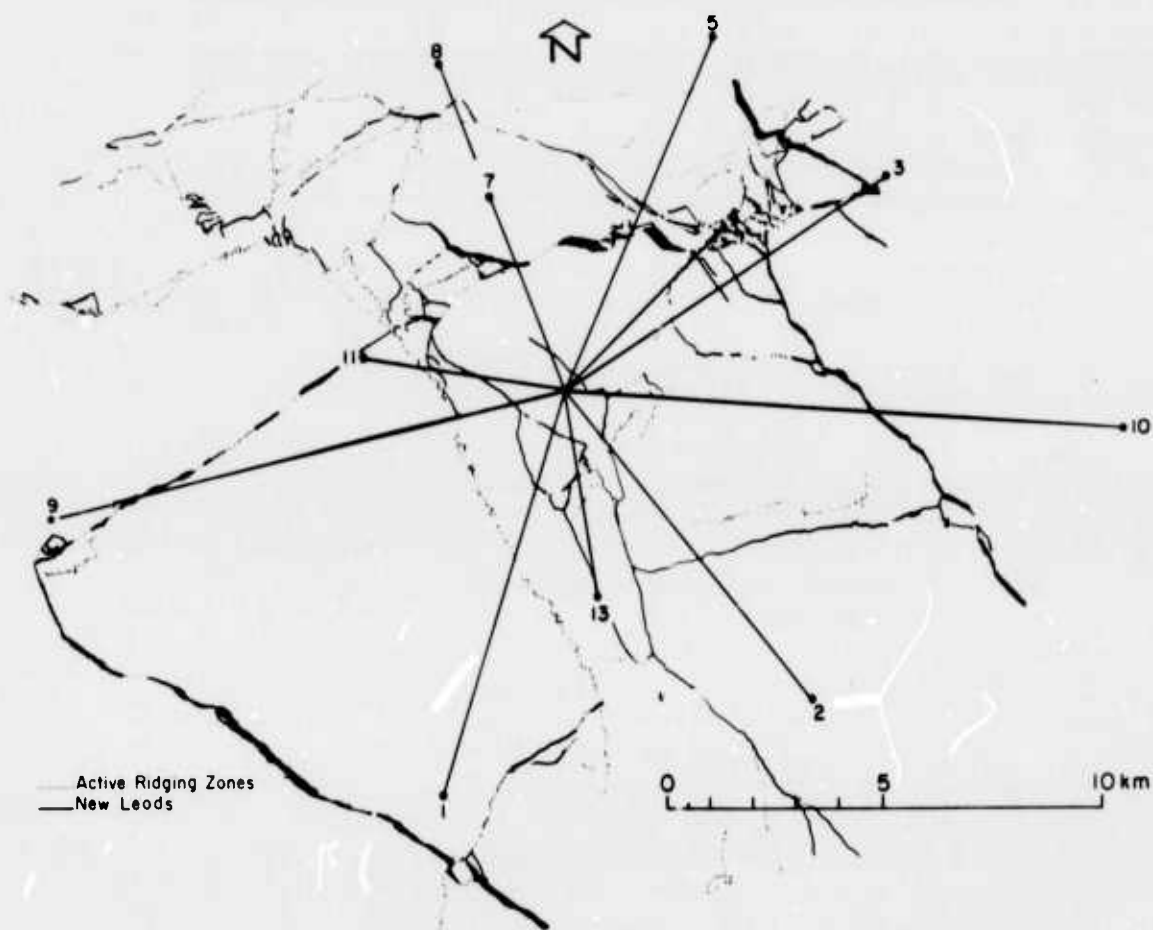


Figure 1. Schematic diagram of the mesoscale strain array together with active leads and ridging zones. Leads and ridges were obtained from a 1500-m aerial photo mosaic taken on 6 April 1972.

case of the pack ice, however, the fluctuations are probably not due so much to random motion of floes (although this is undoubtedly a factor) as to the fact that the floe sizes are large relative to our measurement scale and thus spatial velocity profiles are of a stepwise nature. This is illustrated by Figure 1, which shows that the distance between leads, where relative motion occurs, is generally 4 to 6 km. Also, for pack ice, the fluctuations are expected to be highly variable in time, since they are primarily driven by the transfer of energy into the pack by meteorological forces. This is opposed to a fluid in a laboratory in which fluctuations are well described by the temperature.

As we examine spatial variations in the velocity field over larger and larger areas, the contributions of fluctuations to average velocity differences (i.e. strain rates) would be expected to become less pronounced. Stated differently, the contribution of fluctuations to the sea ice strain rate would be expected to become small when the area covered by the strain array becomes large relative to floe size and/or distances between leads.

In order to sort out the fluctuations from the continuum motion, we analyzed the position data of the mesoscale targets by fitting a least squares planar surface to the spatial velocity field sampled by the array, with the slope angles of the plane representing the strain rate and vorticity. Such a procedure is commensurate with the discussion of sea ice strain by Nye (1973), who notes

that for a precise measure of the strain rate the velocity field needs first to be smoothed before derivatives are taken. Since the area covered by the mesoscale array is relatively small ( $\approx 20$  km in diameter) compared with meteorological systems, we would expect the continuum velocity to be relatively linear over this region and hence the planar approximation should be good. Residual deviations from this planar surface are identified as fluctuations. These residual deviations also cause some uncertainty in the strain rates, an uncertainty which can be estimated by dimensional analysis for different sized arrays on the assumption that the fluctuation amplitude is reasonably similar over the region. As part of this procedure to delineate the difference between continuum motion and fluctuations, we also estimated a continuum length, defined as the length over which, on the average, the continuum velocity differences equal the fluctuation amplitude. This length, which is about 10 km, gives a rough measure of the scale above which sea ice may be viewed as a continuum and below which the discrete nature of the pack begins to dominate the motion.

Finally, in addition to such a least squares analysis for determining scaling effects, we also 1) compared strains obtained from triangles of different sizes ( $\approx 5$  km to  $\approx 20$  km) and 2) compared the mesoscale strain results over the 20-km region with the macroscale strain results obtained from a 100-km triangle, one corner of which was the center of the mesoscale array. These comparisons generally indicated that all arrays were measuring similar continuum motions of the pack, with the fluctuations yielding a large contribution to, but not masking, the continuum motion on a scale of about 20 km.

#### Site Location and Data Collection Procedures

The measurements used for this study were made in the vicinity of the main 1972 AIDJEX camp, located at roughly  $75^{\circ}00'N$ ,  $148^{\circ}30'W$ . The camp, as well as the different research programs conducted from it, are described in AIDJEX Bulletin no. 14 (Thorndike et al. 1972). The strain array was established by erecting a series of targets which consisted of corner cubes mounted on the tops of aluminum poles. The distances to, and angles between, the targets were measured using a continuous wave laser rangefinder. The height of the targets varied from 3 to 10 m above the ice surface depending on the distance and the obstructions between the targets and the main camp. A diagram of the strain array, together with an overlay of active leads and ridging zones, is shown in Figure 1. The angles between the targets were measured with an average accuracy of better than  $\pm 1$  min and were referenced to a fixed stake on the multiyear floe on which the main camp was sited. The line between the laser and the stake was then tied into the true north determinations (sun shots) made by Thorndike and Gill (Thorndike et al. 1972). Distances were measured to the nearest 0.03 m (0.1 ft) because the large strains that were experienced obviated the need for any greater precision.

This strain measurement system was found to be vastly superior to manned tellurometer sites (Hibler et al. 1973a). With this system, a large number of strain lines could be determined easily without manning the remote stations. It was also relatively quick and easy to install, and placed a minimal reliance upon "black boxes." However, visibility problems (wind-blown snow, sea smoke from leads) made acquisition of continuous, equally spaced time series difficult (laser measurements were impossible approximately 10% of the time, and once high winds caused a gap of almost two days in the strain line time series). In addition, the system required manpower 24 hours a day.

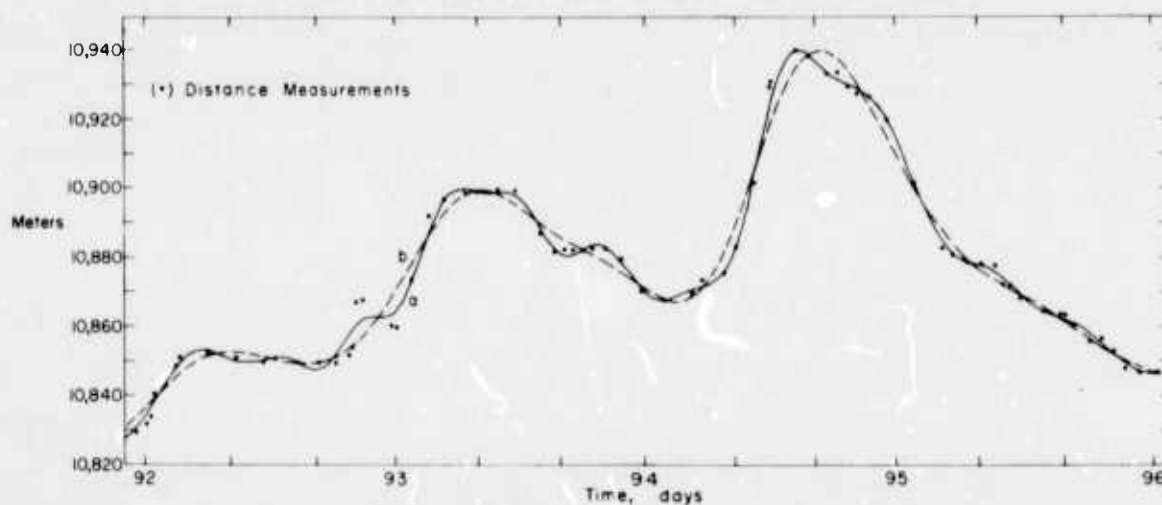


Figure 2. Typical results of the interpolation and smoothing process used to generate equispaced values for the strain analysis. Curve a was obtained with a smoothing filter transition band from 8.0 to 6.15 hours, and curve b with a transition band from 20 to 11.4 hours.

### Data Analysis

#### Extrapolation and smoothing of strain data

Data taken in the field consisted of distances and angles of targets relative to a fixed reference stake. As a first step in the data reduction, these angles were converted to angles relative to true north as measured on Julian day 81 (21 March). Rotations of the array were not taken into account for strain calculations, so that the coordinate system used for this study is slightly different from the true north coordinate system (the maximum difference is, however, less than  $5^\circ$ ). Rotations of the array were included in the vorticity calculations. The time scale was converted to GMT by using four GMT calibration times obtained in the field to find a least squares rate for the clock used in the measurements. The data point times were recomputed with this rate and then all data (both angles and distances) were linearly interpolated and resampled every hour. Using this new data set at 1-hour intervals, the time series was smoothed with a low pass filter having a transition band width with periods from 8.0 to 6.15 hours. The smoothed time series was then resampled every third hour. If there was reason to expect that the data contained a large number of time intervals greater than 3 hours, a low pass filter having a transition band from 20 to 11.4 hours was used before resampling. Both filters had less than 0.6% side lobe errors and consisted of 81 symmetric weights designed according to the procedure discussed by Hibler (1972).

This process of interpolation, followed by smoothing, maybe viewed as a consistent way of constructing a smooth curve (with no high frequency components past a reasonable cutoff dictated by the average sampling rate) through the randomly spaced data points. Alternatively the curve may be considered an accurate representation of the low frequency portion of the linearly interpolated curve.

Examples of the smooth curves generated by this process are shown in Figure 2. Curve a, which results from the filter with the higher frequency cutoff, follows the data quite closely. This indicates that there is little variance associated with periods shorter than 6 hours.



### Experimental error estimation

The primary source of error in the measurements was the uncertainty of target angles. Since angular measurements were generally accurate to  $\pm 0.0003$  radians ( $\pm 1$  min) and distance errors were small, we estimated the  $x$  and  $y$  position errors of each measurement of a target at distance  $r$  and angle  $\theta$  to be

$$\begin{aligned}\Delta x &= 0.0003 r \sin \theta \\ \Delta y &= 0.0003 r \cos \theta.\end{aligned}\tag{1}$$

Since measurements 3 hours apart were subtracted to obtain velocities  $v$ , we estimated  $x$  and  $y$  velocity errors to be

$$\begin{aligned}\Delta v_x &= 0.0006 r \sin \theta / \Delta t \\ \Delta v_y &= 0.0006 r \cos \theta / \Delta t\end{aligned}\tag{2}$$

with  $\Delta t = 3$  hours. This is a slight overestimation of errors for the difference between two numbers with uncorrelated errors. However, since there may have been some errors – due to interpolation between nonequally spaced points – that were not removed by smoothing, we have made a conservative error estimation. The experimental errors given by eq 2 were then used as input to obtain the experimental error on the strain rate tensor, as discussed in the next section.

### Least squares computational technique

To understand conceptually the least squares strain and vorticity calculations, it is useful to visualize a contour plot of the  $x$  (or  $y$ ) velocity component of the ice. In essence, the computer program used to calculate the deformation rate fits a planar surface through the contour plot with the slope angles of the planes yielding the strain rates and vorticities. Since the actual velocity components deviate from a perfect plane, there is some uncertainty in the slope angles of the plane. We refer to the average deviation of the velocity components from the plane as the *residual fluctuation error* and the uncertainty in the slope angles of the plane as the *inhomogeneity variation*. In addition, once the least squares equation for the plane as a function of, say  $N$ , velocity measurements is determined, the estimated experimental errors may be used as input to obtain estimates of slope uncertainties due only to experimental errors. The remainder of the slope uncertainty may then be identified with nonlinearities in the ice velocity field.

To formulate this conceptual model mathematically, we proceed as follows. Using tensor notation for the strain rate, the strain rate tensor  $\dot{\epsilon}_{ij}$  and vorticity  $w$  are defined by

$$\begin{aligned}\dot{\epsilon}_{ij} &= \frac{1}{2} \left( \frac{\partial v_i}{\partial x_j} + \frac{\partial v_j}{\partial x_i} \right) \\ w &= \frac{1}{2} \left( \frac{\partial v_2}{\partial x_1} - \frac{\partial v_1}{\partial x_2} \right)\end{aligned}$$

where  $v_i$  is the  $i$ th velocity component of the ice pack (considered as a continuum) and  $i, j = 1, 2$ , since we are only concerned with the horizontal motion of the sea ice. Considering  $N$  targets whose positions are being measured, we denote by  $v_j^{(i)}$  the measured  $j$ th velocity component of the  $i$ th target, and by  $\theta_i$  and  $r_i$  the polar coordinates of the  $i$ th target relative to an arbitrary origin.

As a model to explain the velocities of the  $N$  targets, we consider the ice velocity field (on the scale of about 20 km) to consist of a continuum velocity component, which varies in a uniformly linear manner (specified by  $\epsilon_{ij}$  and  $w$ ), and a random fluctuation component. Mathematically our model is expressed by the equation

$$u_i = x_{ij} \epsilon_j + z_i \quad (3)$$

where

$$u_i = \begin{cases} v_1^{(i)}, & i = 1 \text{ to } N \\ v_2^{(i-N)}, & i = N + 1 \text{ to } 2N \end{cases}$$

$$x_{ij} = \begin{cases} [r_i \cos \theta_i & r_i \sin \theta_i & 0 & 0 & 1 & 0], & i = 1 \text{ to } N \\ [0 & 0 & r_i \cos \theta_i & r_i \sin \theta_i & 0 & 1], & i = N + 1 \text{ to } 2N \end{cases}$$

$$\epsilon_j = \begin{cases} \epsilon_{11} \\ \epsilon_{12} - w \\ \epsilon_{12} + w \\ \epsilon_{22} \\ A_1 \\ A_2 \end{cases}$$

and  $A_1, A_2$  are constants representing the continuum velocity components at the origin. In eq 3,  $z_i$  is the fluctuation component plus any measurement error and  $E(u_i) = x_{ij} \epsilon_j$  is the "expected" value of  $u_i$ , since  $E(z_i) = 0$ . The least squares estimates of  $\epsilon_i$ , denoted by  $\hat{\epsilon}_i$ , are obtained by minimizing  $\sum z_i^2$ .

To do this, we differentiate  $\sum_{i=1}^{2N} (u_i - \epsilon_j x_{ij})^2$  with respect to  $\epsilon_k$  which yields the matrix equation for the least squares estimates of  $\epsilon_i$  (Jenkins and Watts 1969, p. 131):

$$\hat{\epsilon} = M^{-1} \bar{X}' U \quad (4)$$

where  $M = \bar{X}' \bar{X}$  and prime denotes transposes.

When using these least squares equations, note that adding a constant rotation to all angles only changes the vorticity  $w$ . This can be demonstrated by noting that in eq 3 changing  $w$  to  $w + \theta$  changes  $u_i$  to  $u_i'$  where

$$u_i' = \begin{cases} u_i - (\sin \theta_i) \dot{\theta} r_i & i = 1 \text{ to } N \\ u_i + (\cos \theta_i) \dot{\theta} r_i & i = N + 1 \text{ to } 2N. \end{cases}$$

This, however, is equivalent to adding a constant rotation to all angles. In a similar manner, adding a constant velocity to all points changes only  $A_1$  and  $A_2$ .

Since we have only a finite number of random velocity measurements (each with some random fluctuation "error") to calculate  $\hat{c}_1$ , there is some uncertainty or error in  $\hat{c}_1$ . To estimate this variation or uncertainty, it is necessary to calculate the covariance matrix of  $\hat{c}_1$ , which is easily shown to be given by (Jenkins and Watts 1969, p. 134)

$$C = M^{-1} \bar{X} V \bar{X} (M^{-1}) \quad (5)$$

where  $C_{ij} = \text{cov}(\hat{c}_i, \hat{c}_j)$  and  $V_{ij} = \text{cov}(z_i, z_j)$ . In our case  $z_i$  consists of two parts

$$z_i = z_i^M + z_i^I$$

where  $z_i^M$  is the measurement error (which we estimate to be given by eq 2) and  $z_i^I$  is the fluctuation component of the ice motion, since the actual ice velocity field is nonlinear. If we assume that  $z_i^M$  and  $z_i^I$  are uncorrelated, then the variation in  $\hat{c}_1$  due only to measurement errors, call it  $C_{ij}^M$ , may be estimated using eq 5 with  $V_{ij}^M = \text{cov}(z_i^M, z_j^M)$ . Using eq 2 we estimate  $V_{ij}^M$  to be

$$V_{ij}^M = \delta_{ij} \begin{cases} (\sin \theta_1)^2 r^2 (\Delta \theta / \Delta t)^2, & i = 1 \text{ to } N \\ (\cos \theta_1)^2 r^2 (\Delta \theta / \Delta t)^2, & i = N + 1 \text{ to } 2N. \end{cases} \quad (6)$$

To find the variation of some linear combination of the  $\hat{c}_1$  due to the total "error"  $z_i$ , we make the usual assumption that  $z_i$  are uncorrelated with the same mean and variance so that  $\text{cov}(z_i, z_j) = \delta_{ij} \sigma^2$  where the point estimator of  $\sigma^2$  (denoted by  $s^2$ ) is given by the residual error

$$s^2 = \sum_{i=1}^{2N} \frac{(u_i - \hat{u}_i)^2}{2N - 6} \quad (7)$$

where  $\hat{u}_i = x_{ij} \hat{c}_j$ .

In this case eq 5 reduces to

$$C_{ij} = (M^{-1})_{ij} \sigma^2. \quad (8)$$

Given a linear combination of  $\hat{c}_1$ ,  $\hat{b} = a_i \hat{c}_i$ , then the deviation of  $\hat{b}$  from  $E(\hat{b})$  is such that

$$\hat{b} - E(\hat{b}) / s \sqrt{a_i a_j (M^{-1})_{ij}} \quad (9)$$

has the  $t$  distribution with  $2N-6$  degrees of freedom, assuming that the errors are normally distributed (Bennett and Franklin 1954, p. 250). Consequently, confidence limits for the estimated strain may be obtained using a  $t$  distribution table.

In addition, to the estimated strain, we are also concerned with the velocity fluctuation component  $z_i^I$ , which is strictly speaking not an error, but represents the variation from linearity of the velocity field over the region sampled. In the cases we have studied, the estimated residual error  $z_i$  obtained from eq 7 was generally found to be larger than the average estimated value of experimental error  $z_i^M$  from eq 2. Consequently, as a matter of convenience, we will often refer to the residual error obtained from eq 7 as the residual fluctuation error.



Also, as a matter of notation, we will refer to the uncertainty in  $\hat{\epsilon}_1$  ( $\sqrt{\text{cov}(\hat{\epsilon}_1)}$ ) as the inhomogeneity error. It should be remembered that the inhomogeneity error is an estimate of the uncertainty in the least squares estimated strain and consequently depends somewhat on the number of samples used. The residual fluctuation error, on the other hand, should be relatively independent of the number of sample points used.

### Strain Results

For comparison, strain rate and vorticity time series have been calculated using several different combinations of targets; Table 1 describes all combinations of targets used in the calculations. The origin was also considered a position measurement in some arrays, with distance and angle being zero for all time.

Over the time interval studied in this paper, there was only one major gap in the time series, and this portion is blanked out in the plots. However, for spectral studies, root-mean-square (rms) error estimation, and correlation studies, the whole curve was used (data points every 3 hours), including linearly extrapolated data through the gap, with the linear extrapolation being done on each target position as discussed previously.

**Table 1. Strain line combinations used in this paper.**

Array "name"	Targets	Approximate diameter of region sampled (km)
Combined array	1, 2, 3, 8, 9, 4, 7, 11, 13, 5, 10, origin	20
Outer array	1, 2, 3, 8, 9, origin	20
16-km triangle	2, 5, 9	16
8-km triangle	11, 13, 4	8
5-km triangle	11, 7, origin	5

### Strain tensor time series

Since the outer array targets were measured more often than other targets, the outer array provides a more detailed time series for analysis. Results of least squares calculations using the outer array are shown in Figures 3 and 4, which present the two invariants (Nye 1957) (denoted by  $\dot{\epsilon}_1$  and  $\dot{\epsilon}_2$ ) of the strain rate tensor both separately and in the form of the divergence rate  $\dot{\epsilon}_{11}$  (sum of the principal axis components) and the maximum shear rate  $(\dot{\epsilon}_1 - \dot{\epsilon}_2)/2$  (difference between the principal axis components divided by 2). For the strain rates, the angles of the strain lines at the beginning of each 3-hour interval were used in the least squares calculations. The continuous errors in Figures 3 and 4, the  $\Delta$  values shown below each curve, represent the inhomogeneity error (calculated using eq 7 and 8), which is due primarily to velocity fluctuations. The small error bar on the divergence rate curve represents the maximum experimental error, which was calculated by first calculating the experimental error for each point in the time series according to eq 5 and 6 and then finding the maximum error over the time series. For a more compact summary of the relative magnitude of the strain rates and strain rate variation errors, we list the root-mean-square (rms) values for the various time series in Table II.

## DIFFERENTIAL SEA ICE DRIFT

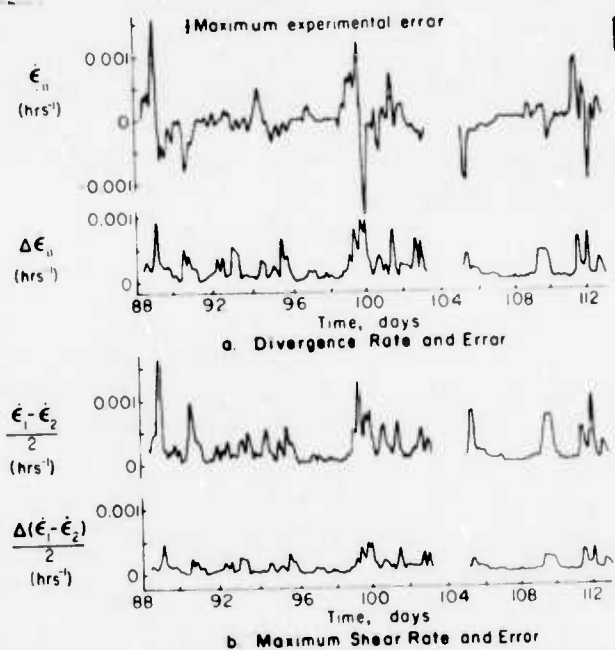


Figure 3. Least squares divergence rate and accompanying inhomogeneity error, and maximum shear rate and inhomogeneity error. The small error bar in a represents the maximum uncertainty due to measurement error.

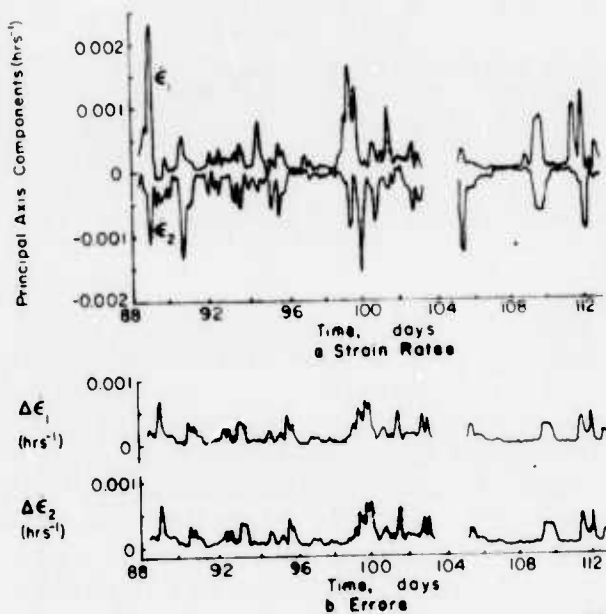


Figure 4. Principal axis components of the least squares strain rate tensor and inhomogeneity errors.

**Table II. Root-mean-square strain rates, strain rate variation errors and experimental errors for combined array.**  
(Units  $10^{-4} \text{ hr}^{-1}$ ).

$i_1$	$\Delta i_1$	$i_2$	$\Delta i_2$	$i_{11}$	$\Delta i_{11}$	$\Delta i_{11} \text{ (exper)}$	$(i_1 - i_2)/2$	$\Delta[(i_1 - i_2)/2]$
4.03	1.92	3.66	1.94	3.28	2.78	0.85	3.48	1.36

From Figures 3 and 4 and Table II, we see that in general strain rates are of greater magnitude than their respective strain rate inhomogeneity errors. The figures also indicate that the inhomogeneity errors generally increase with increasing strain rate. It is important to remember that the inhomogeneity errors shown are for 6 targets and would be smaller for a larger number of targets. This is analogous to the error on the slope of a simple least squares line which becomes less as more points are added even though the standard error of the estimate may remain the same. In particular, for the same residual error for each velocity, an equilateral strain triangle would have a divergence rate error 1.7 times as large as that shown in Figures 3 and 4.

One striking aspect of the deformation, best illustrated in Figure 4, is that in the principal axis coordinate system most of the expansion or contraction is taking place along one axis. Moreover, there is usually contraction along one axis and extension along another. Another salient characteristic of the ice deformation is that the ice motion appears to consist of deformational events which occur every several days and usually consist of dilation followed by convergence.

The strain rate time series generally shows rather rapid variations in strain which are probably due to the random bumping and yielding of floes as well as the random opening of leads. Under our idealized model, consisting of ice fluctuations superimposed upon a continuum, these high frequency motions should primarily represent fluctuations. With respect to maximum strain rates, the maximum observed divergence rate is  $0.16\% \pm 0.09\%$  per hour with a maximum convergence rate of  $0.15\% \pm 0.09\%$  per hour. The largest maximum shear rate is  $0.16\% \pm 0.05\%$  per hour.

#### **Nonlinear velocity fluctuations**

The least squares calculation, besides yielding the average strain rates, also gives a measure of the nonlinearity in the velocity field through the residual fluctuation error. This residual error can be viewed as a fluctuation in the velocity field from the ideal continuum value. The magnitude of these fluctuations is important in determining the size of a measurement array necessary to measure accurately the average strain rate. In terms of our continuum model, the fluctuation contribution, together with the average strain rate, yields a characteristic length above which the pack ice may be considered a continuum and under which the ice motions of individual floes and leads become dominant. Such a characteristic length is estimated by determining the length over which the fluctuation on the average is almost the same as the continuum velocity variations.

For a best estimation of the fluctuation error, we utilized the combined array consisting of 11 targets plus the origin. Since some targets in the combined array were not measured as frequently as those in the outer array, the linearly extrapolated data were smoothed with a filter having a transition band from 20.0 to 11.4 hours, as discussed in the previous section on data analysis (p. 5).

The resulting residual errors from the combined array, and strain tensor components in a (north, west) coordinate system are shown in Figure 5. In order to put the residual error and deformation rates in perspective with the overall motion of the pack ice, plots of the velocity

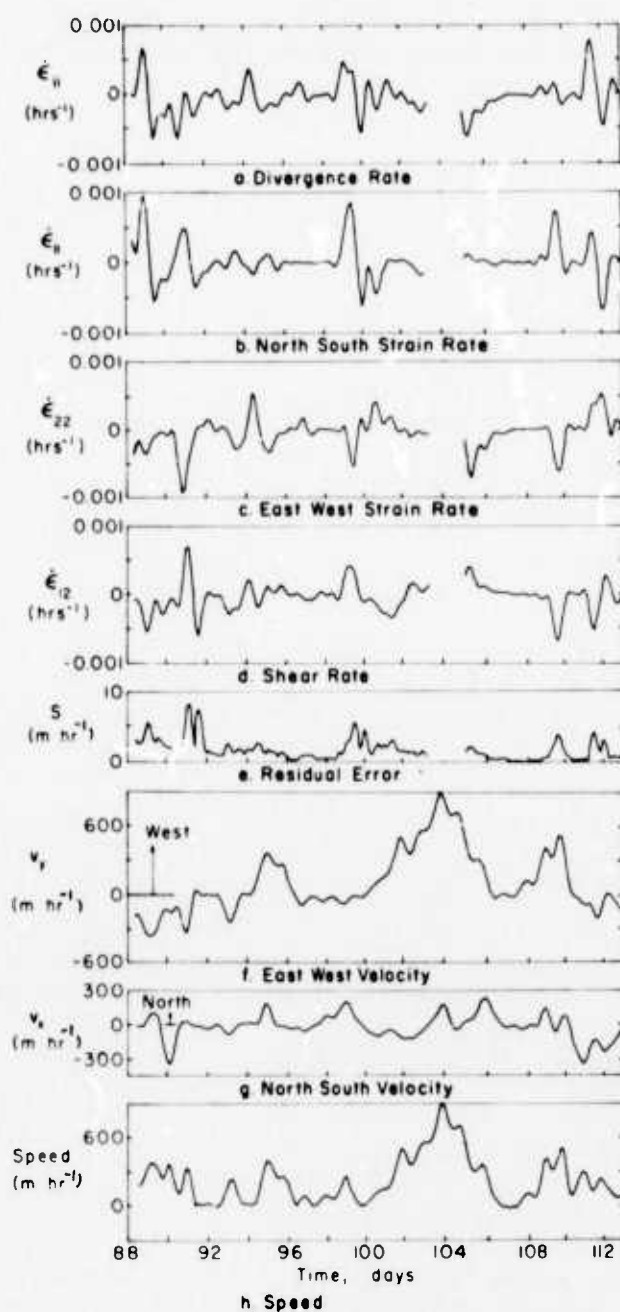


Figure 5. Comparison of mesoscale divergence rate, north-south strain rate, east-west strain rate, shear rate, least squares residual fluctuation error, east-west velocity of the camp, north-south velocity of the camp, and speed of the camp. All curves were smoothed with a low pass filter having a transition band from 20.0 to 11.4 hours.

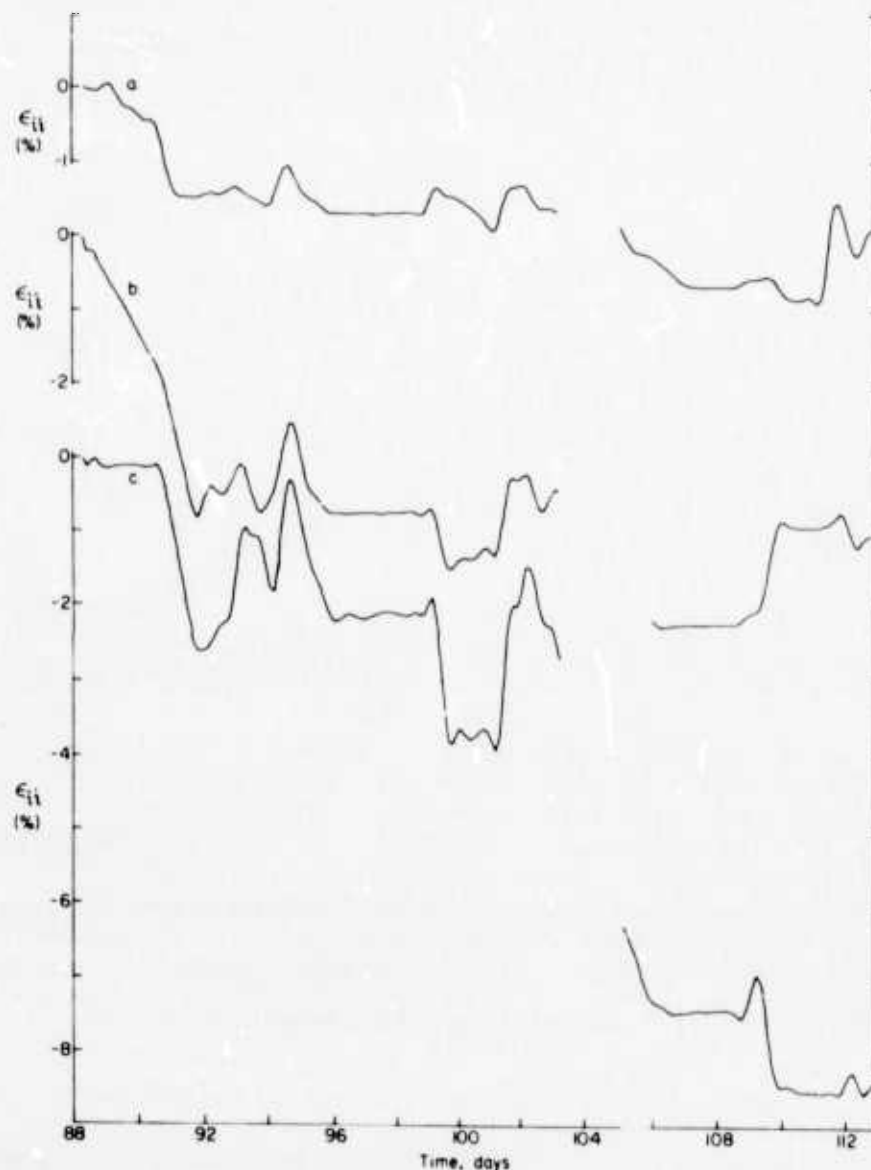


Figure 6. Comparison of net divergences (areas) of overlapping triangles.  
a) 16-km triangle, b) 8-km triangle, c) 5-km triangle.

components of the central point of the array are also shown in Figure 5. These velocity plots were obtained using drift data obtained by Thorndike (1973) from satellite navigation fixes. The velocity data were smoothed with the same filter used in the strain calculation. In the processing of the data carried out by Thorndike, some smoothing was also done, but this smoothing affected only the higher frequencies past the transition band of our filter. For a more concise comparison of the data, rms values of the various curves are given in Table III.

As can be seen from Table III, the characteristic length (residual error/strain rate) over which the velocity change due to strain rate is of the same magnitude as the residual fluctuation error is of the order of 10 km. A second characteristic length of some interest is the length over which the velocity difference according to the strain rate equals the average drift velocity. This length is of the order of 1000 km, roughly similar to the size of the Pacific Gyre. Consequently, the residual



**Table III. Root-mean-square strain rates, residual errors, and central point velocities (from Fig. 5).**

Div rate (hr <sup>-1</sup> )	$i_{11}$ (hr <sup>-1</sup> )	$i_{22}$ (hr <sup>-1</sup> )	$i_{12}$ (hr <sup>-1</sup> )	Residual error (m hr <sup>-1</sup> )	East-west vel (m hr <sup>-1</sup> )	North-south vel (m hr <sup>-1</sup> )	Speed (m hr <sup>-1</sup> )
2.36 (10 <sup>-4</sup> )	2.60 (10 <sup>-4</sup> )	2.37 (10 <sup>-4</sup> )	2.12 (10 <sup>-4</sup> )	2.27	292.3	107.9	312.9

error is rather insignificant in terms of the absolute velocity for a point, but becomes more critical in terms of the velocity gradient or deformation rate. In terms of a continuum model, the results suggest that on a scale larger than about 10 km the pack ice begins to behave like a continuum, whereas on a smaller scale the individual particle behavior begins to dominate the observed motion.

The magnitude of the residual error also allows an estimate to be made of the effect of fluctuations on strain rates from arrays of different sizes. For example, we can view the strain measured by a simple area, say a triangle, to consist of two components: 1) the continuum strain rate and 2) the fluctuation component. Assuming that the residual error is approximately constant, independent of the size of the triangle, then the fluctuation contribution to the strain rate is of greater relative magnitude for small triangles. In addition, since the fluctuation component would be expected to consist of rather rapid bumping motions, strain rates would behave in a more erratic manner as the measuring triangle becomes smaller. This effect is apparent in plots of individual triangles. Figure 6, for example, illustrates the net divergences (essentially the areas) of three nested triangles as a function of time. The more rapid, large-magnitude motion of the small triangles is apparent. The curves do, however, illustrate a general correlation of strain events consisting of dilation followed by convergence. Generally these results suggest that, although the smaller triangles are averaging over very few leads and/or floes, over a period of several days the ice on a small scale would be expected to diverge if the pack is generally diverging and converge if the pack is converging.

#### Comparison of Mesoscale Deformation with Macroscale Deformation

In addition to a satellite navigation system at the main 1972 AIDJEX camp (the center point of the mesoscale array), the 1972 pilot study included satellite position measurements of two other camps approximately 100 km west and northwest, respectively, of the main camp. Strain data from this larger triangle, referred to as *macroscale deformation*, provide a valuable measure of the deformation averaged over a larger region than that covered by the mesoscale array.

In a comparison of the macroscale and mesoscale deformation rates, arguments for both similarities and differences can be made. First, since weather systems typically vary over several hundred kilometers, we would intuitively expect some similarity between the macro- and mesoscale deformation rates, at least to the extent that both systems are measuring the continuum motion of the ice pack. However, there are several reasons why the correlation should not be extremely good. Foremost is the fact that the mesoscale array is only slightly larger than the estimated continuum length of 10 km and thus fluctuations of the velocity field yield a strong component in the least squares mesoscale deformation time series, a much stronger component than would be expected to be present in the macroscale data. Also, even if the pack ice could be considered a homogeneous continuum at very small scales, the nature of the continuum constitutive law might couple with variations in the weather systems to give rapid variations in the deformation. This is especially true since the mesoscale array is not at the center of the macroscale array, but at one corner of it.

In order to examine differences and similarities between the macroscale and mesoscale deformation, and thus test some of the above hypotheses, a comparison of the various deformation time series and their spectra was made. The macroscale deformation data were supplied by Thorndike and are essentially the same data as presented by him (Thorndike 1973). In the processing of the macroscale data, Thorndike employed a Kalman filtering procedure to obtain this position and velocity of each of the three satellite sites. The filter cutoffs varied somewhat but generally all frequencies up to about 18-hour wavelengths were passed. The strain rates and vorticities were uniquely determined since there were only three stations.

#### Time series comparison

In order to smooth both time series in the same manner, all deformation rates were smoothed with a low-pass filter with a transition band from 21 to 84 hours. This smoothing also allowed a mesoscale vorticity time series to be constructed by including the camp rotation, a step that was difficult without extensive smoothing because azimuthal measurements were typically made only once a day. To obtain the camp rotation for the mesoscale calculation, a time series  $R = (\sin \phi)$  longitude - azimuth [with longitude increasing in an easterly direction, see Nye (1974)] with  $\phi$  the latitude was constructed by linearly extrapolating the satellite position and azimuth measurements reported by Thorndike et al. (1972). This time series was smoothed by using the same filter that was applied to the deformation data and differentiated to obtain a rotation rate. This rotation rate was added to the vorticity calculation in the camp coordinate system to obtain the true vorticity as discussed in a previous section. For mesoscale data in the camp coordinate system, the outer array least squares results were used. In addition, several days of earlier data (taken before the array was complete), consisting of only 4 targets (1, 2, 3, 8) and the center point, were used to extend the time series.

Figure 7 gives a comparison of mesoscale and macroscale divergence rates, vorticities and maximum shear rates. Because of a malfunction of one of the satellite navigation units, there is a several-day gap in the macroscale data which was bridged by Thorndike (1973) using a Kalman filter. This gap is denoted by vertical lines enclosing *interpolated macro data* in Figure 7. For a quantitative comparison of the curves, we give in Table IV correlation coefficients and root-mean-square (rms) values for the various curves up to the gap in the macroscale data. The standard error for the correlation coefficients is based upon a number of degrees of freedom equal to the number of points correlated times the fraction of the spectrum passed by the filter.

Figure 7 and Table IV indicate that there are significant correlations between the deformation time series measured at different scales. Visual examination of the curves suggests that the correlation is due to the presence of similar strain events over several-day periods. However, since these events are often of different amplitudes and occur at slightly different times, the correlation is not complete, especially at higher temporal frequencies. The results also show that the deformation rates have comparable amplitudes with the mesoscale amplitude generally being slightly larger. The comparison generally indicates that both meso- and macroscale arrays are measuring similar continuum motions of the ice pack.

**Table IV. Meso- and macroscale root-mean-square deformation rates and correlation coefficients (from Fig. 7).**

	Divergence rate		Vorticity		Maximum shear	
	Meso	Macro	Meso	Macro	Meso	Macro
Root-mean-square ( $10^{-4} \text{ hr}^{-1}$ )	2.84	2.28	4.37	2.45	3.73	2.37
Correlation coefficient	$0.47 \pm 0.20$	$0.47 \pm 0.20$	$0.71 \pm 0.20$	$0.71 \pm 0.20$	$0.38 \pm 0.20$	$0.38 \pm 0.20$

## DIFFERENTIAL SEA ICE DRIFT

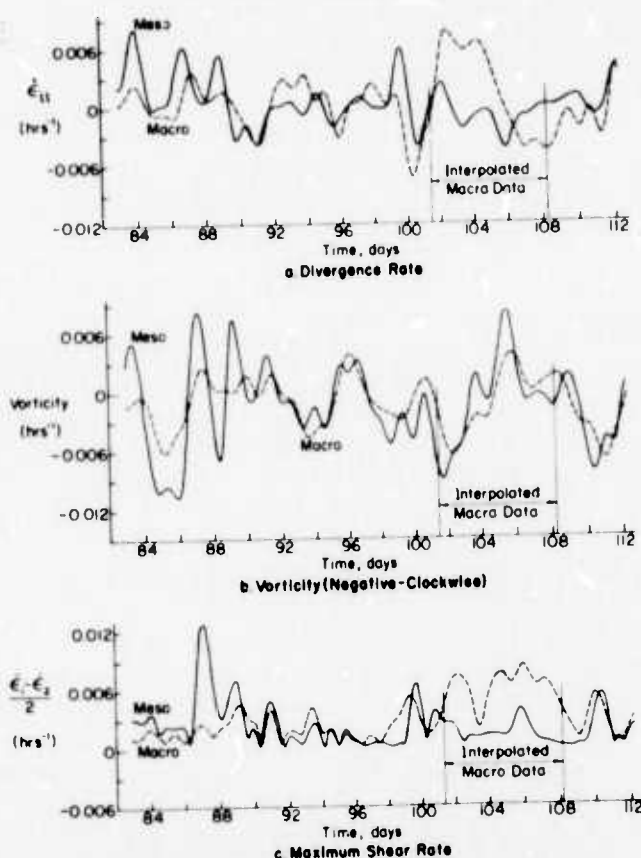


Figure 7. Comparison of mesoscale and macroscale divergence rates, vorticities, and maximum shear rates. The dashed lines represent macroscale data and the solid lines mesoscale data.

## Spectral densities

Some of the important differences between the nature of the mesoscale deformations and that of the macroscale deformations are illustrated by the spectral densities which we calculated using the lag product method as discussed, for example, by Rayner (1971, p. 94). Figure 8a shows the spectra of the mesoscale divergence rate and shear rate (*not* maximum shear), and Figure 8b shows the spectra of the macroscale divergence rate, shear rate and vorticity. Because of the inadequacy of the camp rotation time series at higher frequencies, it is not possible to construct a mesoscale vorticity spectrum. Also, because of the Kalman filter smoothing of the macroscale data, the macroscale spectra are valid only up to about 15-hour wavelengths. Since there were differing data gaps, the spectra did not come from the same time periods, but were calculated from Julian day 88 to 113 for the mesoscale data, and from Julian day 81 to 101 for the macroscale data.

Figure 8 shows that the macroscale spectra generally contain less variance at higher frequencies than the mesoscale spectra. Such a result is commensurate with viewing the deformation as a continuum signal and a fluctuation component with the fluctuation magnitude dropping off inversely with the size of the array. This follows because the fluctuation signal, being of a random nature, would be expected to have a greater high-frequency variance than the continuum signal.

An interesting aspect of the mesoscale spectra (especially the divergence rate) is the presence of a significant spectral peak at about 12-hour wavelengths. Whether such a peak is contained in



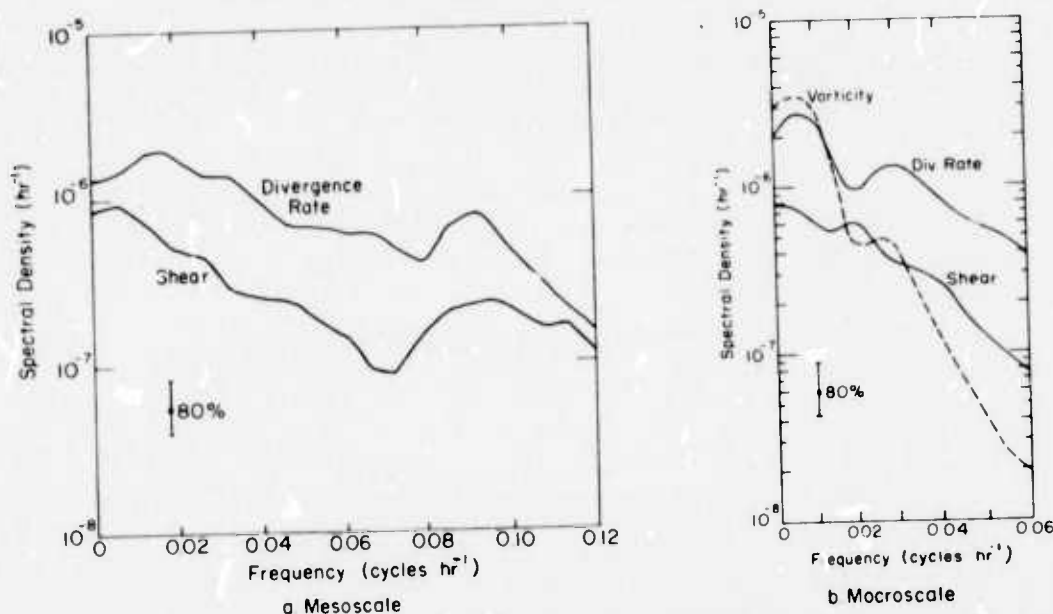


Figure 8. Power spectra of mesoscale divergence rate, and shear rate; and macroscale divergence rate, shear rate and vorticity.

the macroscale data cannot be ascertained because the smoothing employed by Thorndike (1973) effectively filtered out any such oscillation. A possible explanation for this peak is a variation in water currents due to inertial oscillations (Hunkins 1967). Measurements of ocean currents by Newton and Coachman (1973) during previous AIDJEX pilot studies indicated 12-hour cycles in the currents, with the oscillation displaying coherence over distances up to 20 km. Different drag coefficients for different ice floes could couple with these currents to create a differential ice motion. There is also evidence of an  $\approx 24$ -hour cycle in the macroscale divergence rate spectrum (which may possibly be present in the mesoscale data). The source of this peak is not at present understood.

The general fall-off of the spectra in Figure 8 is also relevant for sampling considerations. The shape of the spectra generally suggests that sampling intervals up to 10 hours (with accurate measurements) would yield low frequency information without intolerable aliasing. A more direct test of this can be made by sampling the data at larger intervals before smoothing and comparing the results to data smoothed before resampling. Such comparisons have been made for the mesoscale data (Hibler et al. 1973b) and support the conclusion that accurate samples every 8 hours are adequate for resolving the low frequency components of the time series required for comparison with synoptic meteorological variations which generally occur over a time scale of several days (Monin 1972).

#### Nature of the Ice Pack Rotation

Examination of the mesoscale vorticity indicates that it is similar to the camp rotation. This can be seen from Figure 9, which shows the camp rotation rate and the mesoscale vorticity. This similarity means that to a large degree the whole mesoscale region is rotating as an entity. Investigation of the macroscale deformation data indicates that such a "solid" rotation is also partially occurring for the larger macroscale region, at least at low temporal frequencies. This may be seen from Figure 10 in which the east-west shear rate  $\partial v_y / \partial x$  and vorticity are plotted together. As can be seen, both curves are similar, indicating that  $\partial v_x / \partial y$  and  $\partial v_y / \partial x$  are close to being equal in

## DIFFERENTIAL SEA ICE DRIFT

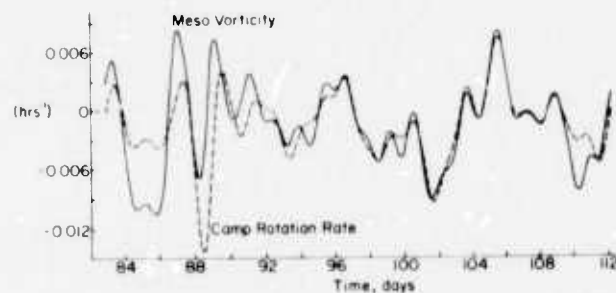


Figure 9. Camp rotation rate and mesoscale vorticity.

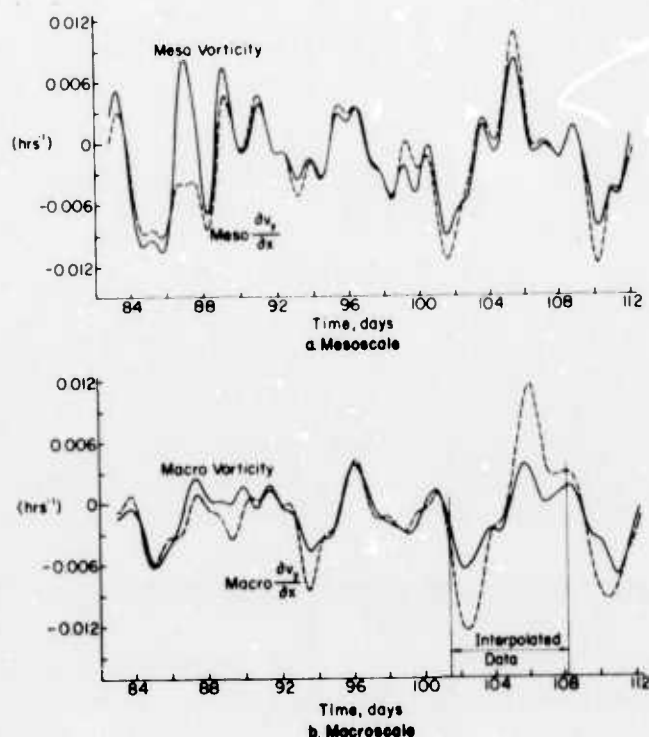


Figure 10. Comparison of east-west shear rate ( $\partial v_y / \partial x$ ) and vorticity.

magnitude and opposite in sign, a condition which holds identically for solid rotation. Another indication of this behavior on the macroscale is the relative smallness at low frequencies of the macroscale shear rate spectral density in the x-y coordinate system compared with the macroscale vorticity spectral density as shown in Figure 8b.

These observations suggest that the most pronounced mode of differential deformation of the ice pack is a relatively cohesive rotation, at least at low frequencies, of the pack. The direction of the rotation is, from the curves in Figure 4, generally clockwise in agreement with the motion of the Pacific Gyre. Other deformation rates at low frequencies appear to be somewhat smaller than the rotation rate. Such a cohesive rotation is also borne out by shear zone deformation studies (Crowder et al. 1974, Hibler et al. 1974), suggesting that the pack is rotating as a relatively tightly bound continuum with slippage at the boundaries.

A final point of interest is a negative correlation between the vorticity and the divergence rate (see Fig. 7). The correlation coefficient for the mesoscale data (omitting the earlier data taken before the mesoscale array was complete) is  $-0.35 \pm 0.17$ , indicating that a convergence is associated with a clockwise rotation. This correlation is discussed in greater detail in relation to linear drift theories and atmospheric pressure variations in Part II of this report.

### Conclusions

We believe that this study has shown that strains measured on a scale of 10 km or greater can serve as a valid measure of the continuum motion of sea ice. When strains are measured on a smaller scale, the continuum motion is obscured by the random bumping and yielding of floes and by the finite size of the interacting floes relative to the size of the strain array. These small-scale motions are, however, interesting in their own right. Our results also indicate that meaningful vorticity values can be obtained from even smaller arrays, indeed from the measured rotation of individual stations.

These results suggest that it should be possible to carry out highly useful experiments on the macroscale (continuum) behavior of pack ice by utilizing one manned drifting station or ship with radar transponders located at the remote strain points. Strain arrays with effective diameters of up to 50 km should easily be possible using currently available techniques.

Finally, it should be emphasized that our results were obtained from a pack ice field with a compactness of near one and a specific, but unknown, ice thickness distribution. Whether similar results would be obtained for other ice conditions, is presently a moot point.

### Literature Cited

- Bennett, C.A. and N.L. Franklin (1954) *Statistical analysis in chemistry and the chemical industry*. New York: J. Wiley and Sons.
- Crowder, W.K., H.L. McKim, S.F. Ackley, W.D. Hibler III and D.M. Anderson (1947) Mesoscale deformation of sea ice from satellite imagery. *Proceedings of the Interdisciplinary Symposium on Advanced Concepts and Techniques in the Study of Snow and Ice Resources* (Monterey, California), National Research Council.
- Hibler, W.D. III (1972) Design of small error low pass filters with arbitrarily sharp frequency cut-offs. U.S. Army Cold Regions Research and Engineering Laboratory (USA CRREL) Research Report 304. AD 750116.
- Hibler, W.D. III (1974) Differential sea ice drift, II: Comparison of mesoscale strain measurements with linear drift theory predictions. *Journal of Glaciology*, vol. 13, no. 68, p. 457-471.
- Hibler, W.D. III, W.F. Weeks, S. Ackley, A. Kovacs and W.J. Campbell (1973a) Mesoscale strain measurements of the Beaufort Sea pack ice (AIDJEX 1971). *Journal of Glaciology*, vol. 12, no. 65, p. 187-206.
- Hibler, W.D. III, W.F. Weeks, A. Kovacs and S. Ackley (1973b) Differential sea ice drift, I: Spatial and temporal variations in mesoscale strain in sea ice. *AIDJEX Bulletin*, no. 21, p. 79-113.
- Hibler, W.D. III, S.F. Ackley, W.K. Crowder, H.L. McKim and D.L. Anderson (1974) Analysis of shear zone ice deformation in the Beaufort Sea using satellite imagery. Symposium on Beaufort Sea Coastal and Shelf Research, Washington, D.C., Arctic Institute of North America.
- Hunkins, K.L. (1967) Inertial oscillations in Fletcher's Ice Island (T-3). *Journal of Geophysical Research*, vol. 72, no. p. 1165-1174.

- Jenkins, G.M. and D.G. Watts (1969) *Spectral analysis and its applications*. San Francisco: Holden Day.
- Monin, A.S. (1972) *Weather forecasting as a problem in physics*. Cambridge: MIT Press.
- Newton, J.L. and L.K. Coachman (1973) Observations of ice motion and interior flow field during 1971 AIDJEX pilot study. *AIDJEX Bulletin*, no. 18, p. 5-30.
- Nye, J.F. (1957) *Physical properties of crystals*. Oxford: Oxford University Press.
- Nye, J.F. (1973) The meaning of two-dimensional strain-rate in a floating ice cover. *AIDJEX Bulletin*, no. 21, p. 9-17.
- Nye, J.F. (1974) The definition of rotation of a drifting ice floe. *AIDJEX Bulletin*, no. 23, p. 40-44.
- Rayner, J.N. (1971) *An introduction to spectral analysis*. New York: Pion Limited.
- Thorndike, A.S. (1973) Analysis of position measurements, AIDJEX 1972. *Transactions, American Geophysical Union*, vol. 53, no. 11.
- Thorndike, A.S., D. Bell, I. Vivsueiks and A. Gill (1972) Station positions, azimuths, weather; 1972 AIDJEX pilot study; Preliminary data. *AIDJEX Bulletin*, no. 14, p. 63-71.

## PART II. COMPARISON OF MESOSCALE STRAIN MEASUREMENTS WITH LINEAR DRIFT THEORY PREDICTIONS

by

W.D. Hibler III

### Introduction

One of the more important uses of mesoscale strain measurements is the comparison of the differential drift, i.e., strain results, with sea ice drift theories, both to test the theories and to determine certain unknown parameters. These comparisons provide a more critical measure of certain constitutive law parameters than do comparisons involving the drift of only a single point. To make such a comparison in this report, a linearized drift theory similar to that used by Egorov (1970, 1971), Rothrock (1972), and Witting (1972) will be used. Such theories, although not as exact as other calculations (Campbell 1965, Campbell and Rasmussen 1973), do suffice for obtaining quantitative estimates of the dominant drift effects.

Recent calculations using linear drift theories have generally been of two types. In the first, as carried out by Rothrock (1972) and Witting (1972) independently, the average yearly circulation of the arctic ice cover has been calculated assuming that the ice is incompressible. Such calculations, although of considerable interest, are not directly comparable to mesoscale strain measurements. In the second, as carried out by Egorov, an approximate infinite boundary solution is obtained to a linear drift theory that uses a shear viscosity to explain the rheological behavior of the ice and neglects gradient current effects, i.e., neglects geostrophic ocean flow below the surface boundary layer. The second approach yields results more directly comparable to strain measurements.

For the comparison made here, a linear drift equation similar to that used by Egorov will be used. The rheological behavior of the ice will be taken into account by using the constitutive law proposed by Glen (1970), which includes a bulk viscosity as well as a shear viscosity. In addition, calculations will be made using a more general linear viscoelastic constitutive law that allows for memory effects and includes a generalized Hooke's law as well as the Glen law as special cases. As in Egorov's work, gradient current effects will be neglected.

However, unlike Egorov, we will formulate the infinite boundary solution without approximation in terms of a linear response function. The resulting real space solution consists of a straightforward integral operator which may be applied to the pressure field to obtain expected differential ice drift. This response function form of the solution is useful because it clearly illustrates the differences of ice drift behavior expected in winter as opposed to that expected in summer. In addition, the solution allows a rapid determination of the scales of variation in the atmospheric pressure field that are important for given bulk and shear viscosity values. Furthermore, the comparison of strain measurements with pressure data allows the bulk and shear viscosity parameters to be estimated.

### List of Symbols

$w$	ice vorticity	$\text{sec}^{-1}$
$\Delta$	ice divergence rate	$\text{sec}^{-1}$

$m$	ice mass per unit area	$\text{kg m}^{-2}$
$u$	ice velocity	$\text{m sec}^{-1}$
$v$	wind velocity	$\text{m sec}^{-1}$
$f$	Coriolis vector	$\text{sec}^{-1}$
$f$	Coriolis parameter equal to magnitude of the Coriolis vector times the sine of the latitude	$\text{sec}^{-1}$
$\lambda$	mf	$\text{kg sec}^{-1} \text{m}^{-2}$
$F$	force due to internal ice stress	$\text{N m}^{-2}$
$\tau_w$	water stress on ice	$\text{N m}^{-2}$
$\tau_a$	air stress on ice	$\text{N m}^{-2}$
$\phi$	Ekman angle in air	dimensionless
$\theta$	Ekman angle in water	dimensionless
$B$	wind stress constant $= \rho(fK_a/2)^{1/2}$	$\text{kg sec}^{-1} \text{m}^{-2}$
$D$	water stress constant $= \rho_w(fK_w/2)^{1/2}$	$\text{kg sec}^{-1} \text{m}^{-2}$
$\rho$	air density	$\text{kg m}^{-3}$
$\rho_w$	water density	$\text{kg m}^{-3}$
$K_a$	eddy viscosity of air	$\text{m}^2 \text{sec}^{-1}$
$K_w$	eddy viscosity of water	$\text{m}^2 \text{sec}^{-1}$
$U_g$	x component of geostrophic wind	$\text{m sec}^{-1}$
$V_g$	y component of geostrophic wind	$\text{m sec}^{-1}$
$P$	atmospheric pressure	mb
$\bar{P}$	spatial average of the atmospheric pressure	mb
$\eta$	shear viscosity of ice	$\text{kg sec}^{-1}$
$\zeta$	bulk viscosity of ice	$\text{kg sec}^{-1}$
$H$	divergence rate response function	dimensionless
$G$	vorticity response function	dimensionless

### Linear Drift Equations

Following Egorov's (1970, 1971) example, we consider a steady state equilibrium drift equation for the case where the gradient current term varies so slowly in space and time that it may be neglected. By neglecting this term, the sea ice is effectively considered to be moving across a stagnant ocean [see, for example, Rothrock (1972)]. In this case the equilibrium equation takes the form

$$-mf \times u + \tau_w + \tau_a + F = 0 \quad (1)$$

where  $u$  is the ice velocity,  $f$  the Coriolis vector,  $m$  the ice mass per unit area,  $F$  the force due to internal ice stress, and  $\tau_w$  and  $\tau_a$  the water and air stresses on ice, respectively. The components of water and air stresses are given by a simple Ekman layer theory:

$$\tau_{ax} = B (\cos \phi U_g - \sin \phi V_g) \quad (2)$$

$$\tau_{ay} = B (+ \cos \phi V_g + \sin \phi U_g)$$

$$\tau_{wx} = D (-\cos \theta u_x + \sin \theta u_y) \quad (3)$$

$$\tau_{wy} = -D (\sin \theta u_x + \cos \theta u_y)$$

where  $\phi$  and  $\theta$  are the Ekman angles in the air and water, respectively. The parameters  $B$  and  $D$  are proportionality constants related to the turbulence coefficients for the atmosphere and the ocean. For the classical Ekman layer solution (Sutton 1953, p. 71),  $B$  and  $D$  are given by  $\rho \lambda f(K/2)$  where  $\rho$  and  $K$  are the air density and eddy viscosity respectively of either air or water.  $U_g$  and  $V_g$  are the geostrophic wind components given by

$$U_g = -\frac{1}{\rho f} \frac{\partial P}{\partial y} \quad (4a)$$

$$V_g = \frac{1}{\rho f} \frac{\partial P}{\partial x} \quad (4b)$$

where  $\rho$  is the air density,  $P$  is the atmospheric pressure and  $f$  is the magnitude of the Coriolis vector. In eq 2 it is implicitly assumed that the ice velocity is small compared with the wind velocity and may be neglected. For  $F$ , the force due to internal ice stress, the constitutive law proposed by Glen (1970) is used:

$$F = \eta \nabla^2 u + \zeta \nabla (\nabla \cdot u) \quad (5)$$

where  $\zeta$  and  $\eta$  are bulk and shear viscosity constants that can vary with ice compactness and therefore season. Calculations using a somewhat more general constitutive law are discussed later.

### Ice Drift Solutions

In this case the interest is primarily in the solutions of the linear drift equations for the ice divergence rate  $\Lambda [\Lambda = (\partial u_x / \partial x) + (\partial u_y / \partial y)]$  and ice vorticity  $w [w = 1/2[(\partial u_y / \partial x) - (\partial u_x / \partial y)]]$ . By taking the divergence and curl of eq 1, two linear equations for  $\Lambda$  and  $w$  are obtained:

$$[(\eta + \zeta) \nabla^2 - D \cos \theta] \Lambda + (\lambda + D \sin \theta) 2w = \frac{B \sin \phi}{\rho f} \nabla^2 P \quad (6)$$

$$-(\lambda + D \sin \theta) \Lambda + (\eta \nabla^2 - D \cos \theta) 2w = \frac{-B \cos \phi}{\rho f} \nabla^2 P \quad (7)$$

where  $\lambda = mf$ . These equations represent a linear system with the input being the pressure field  $P$  and the output being  $\Lambda$  and  $w$ . Such systems (Jenkins and Watts 1968) may be described by response functions in wave number space  $H_1(k)$ ,  $H_2(k)$ , so that  $\tilde{\Lambda}(k) = H_1(k) \tilde{P}(k)$  and  $\tilde{w}(k) = H_2(k) \tilde{P}(k)$  where we denote wave number space functions with a tilde and  $k = |k|$ . The response functions may be obtained straightforwardly by Fourier transforming eq 6 and 7, yielding wave number space equations



$$\bar{\Lambda}(k) = \frac{B}{\rho f} \frac{\bar{P}(k)}{\eta + \zeta} [1 - \bar{H}(k)] \quad (8)$$

$$w(k) = \frac{-B}{\rho f} \frac{P(k)}{2\eta} [1 - \bar{G}(k)] \quad (9)$$

where

$$1 - \bar{H}(k) = \frac{k^2 [(\eta k^2 + D \cos \theta) \sin \phi - \cos \phi (\lambda + D \sin \theta)](\eta + \zeta)}{[\lambda^2 + D^2 + 2D \sin \theta \lambda + (\eta + \zeta) \eta k^4 + D \cos \theta (2\eta + \zeta) k^2]} \quad (10)$$

$$1 - \bar{G}(k) = \frac{k^2 [(\eta + \zeta) k^2 + D \cos \theta] \cos \phi + \sin \phi (\lambda + D \sin \theta) \eta}{[\lambda^2 + D^2 + 2D \sin \theta \lambda + (\eta + \zeta) \eta k^4 + D \cos \theta (2\eta + \zeta) k^2]} \quad (11)$$

By the convolution theorem these equations yield simple integral equations in real space. For example, for  $\Lambda(x)$

$$\Lambda(x) = \frac{B}{\rho f(\eta + \zeta)} [P(x) - P'(x)] \quad (12)$$

where (using polar coordinates)

$$P'(x) = \int_0^\infty H(r - r') \int_0^{2\pi} P(r', \theta) r' d\theta dr' \quad (13)$$

and

$$H(r) = \frac{1}{2\pi} \int_0^\infty \bar{H}(k) k J_0(kr) dk. \quad (14)$$

and  $J_0$  is the zero'th order Bessel function. It should be noted that these equations only apply exactly to an ice cover and pressure field of infinite extent and, in fact, represent solutions using boundary conditions  $P(x)$ ,  $\Lambda(x)$ ,  $w(x)$  finite at  $x, y \rightarrow \pm \infty$ . However, in practice they may be applied to a finite case with the necessary extent of the ice cover and pressure field determined by the spatial extent of a finite filter  $H(r)$  that approximates the wave number response  $\bar{H}(k)$  in eq 10.

The wave number space form of the response functions  $\bar{H}(k)$  and  $\bar{G}(k)$  contains considerable information. In the case of the divergence rate for  $\eta, \zeta$  large,  $1 - \bar{H}(k)$  is generally positive for large  $k$  and negative or zero for small  $k$ . Thus, the divergence rate is essentially the result of a high pass filtering operation on the pressure field with the high wave numbers contributing positively to the divergence rate and the low wave numbers negatively with a smaller amplitude. For the vorticity, the response function is also a high pass filter, but there is no change in the sign of the contribution from different wave number components of the pressure field. The wave number of the filter cutoff decreases as  $\eta$  and  $\zeta$  increase. Thus, different types of behavior are expected for  $\eta, \zeta$  small as compared with  $\eta, \zeta$  large. These different types of behavior may be characterized by examining the two limiting cases  $\eta, \zeta \rightarrow 0$  and  $\eta, \zeta \rightarrow \infty$ .



**Limiting cases**

For the first case, noting that  $[1 - \bar{H}(k)]/(\eta + \zeta)k^2$  and  $[1 - \bar{G}(k)]/\eta k^2$  are finite as  $\eta, \zeta \rightarrow 0$ , we have

$$\lim_{\eta, \zeta \rightarrow 0} \Lambda(\mathbf{x}) = \frac{-B}{\rho f} \nabla^2 P(\mathbf{x}) \frac{[D(\cos \theta \sin \phi - \sin \theta \cos \phi) - \lambda \cos \phi]}{\lambda^2 + D^2 + 2D\lambda \sin \theta} \quad (15)$$

$$\lim_{\eta, \zeta \rightarrow 0} w(\mathbf{x}) = \frac{+B}{2\rho f} \nabla^2 P(\mathbf{x}) \frac{[D(\cos \theta \cos \phi + \sin \theta \sin \phi) + \lambda \sin \phi]}{\lambda^2 + D^2 + 2D\lambda \sin \theta}. \quad (16)$$

Thus, we see the well known result that for equal Ekman angles and small  $\eta, \zeta$  the ice would be expected to diverge in a low ( $\nabla^2 P > 0$ ) and converge in a high, whereas the vorticity would be expected to be positive (counterclockwise) in a low and vice versa in a high.

For the second limiting case, we note that, for  $\eta, \zeta$  very large,  $\bar{H}(k)$  and  $\bar{G}(k)$  pass only the very long spatial wavelengths with the pass band frequency cutoff scaling as  $1/\eta$  and/or  $1/\zeta$ . Consequently, the real space response functions  $H(\mathbf{x})$  and  $G(\mathbf{x})$  approach constants (with integrated areas of unity) for very large  $\eta, \zeta$ . Therefore,  $\int H(\mathbf{x} - \mathbf{x}') P(\mathbf{x}') d\mathbf{x}'$  and  $\int G(\mathbf{x} - \mathbf{x}') P(\mathbf{x}') d\mathbf{x}'$  approach the average pressure for large  $\eta$  and  $\zeta$ ; as a result the large  $\eta, \zeta$  limiting equations are

$$\lim_{\eta, \zeta \rightarrow \infty} \Lambda(\mathbf{x}) = \frac{B}{(\eta + \zeta)f} [P(\mathbf{x}) - \bar{P}] \sin \phi \quad (17)$$

$$\lim_{\eta, \zeta \rightarrow \infty} w(\mathbf{x}) = \frac{-B}{2\eta\rho f} [P(\mathbf{x}) - \bar{P}] \cos \phi \quad (18)$$

where  $\bar{P}$  is the mean atmospheric pressure over the infinite  $x, y$  space which would be approximately constant in time. For  $\eta, \zeta$  large but finite,  $\bar{P}$  would be replaced by the very low wave number components of the pressure field which would be expected to be reasonably constant in time if the cutoff wavelength were longer than the synoptic variation scale of the pressure field.

As can be seen from eq 17 and 18, in the large  $\eta, \zeta$  limiting case the divergence rate and vorticity are proportional to the local pressure deviation from the overall mean pressure with a low pressure indicating a convergence and a positive vorticity. Note that there is no dependence on the water stress in this limiting case. In fact the large  $\eta, \zeta$  case is equivalent to neglecting all stresses except the internal ice stress and wind stress. An alternative derivation, for example, would be to delete the water stress and Coriolis terms from eq 6 and 7 and solve a boundary value problem with  $(\Lambda - P)$  and  $(w + P)$  finite at  $x, y \rightarrow \pm \infty$ . It is also important to note that the large  $\eta, \zeta$  solution includes lateral transfer of stress through the pack up to infinite distances via the  $\bar{P}$  term. However, this term becomes only a constant because the lateral stress averages out and thus  $\Lambda$  and  $w$  follow the local pressure.

To the extent that  $\eta, \zeta$  may be considered very large in the winter and small in the summer, the two limiting cases suggest that sea ice (far from coastal boundaries) would be expected to converge in a low in winter and diverge in a low in summer with vorticity always positive in a low. Such predicted behavior agrees with earlier mesoscale strain measurements (Hibler et al. 1973), with the more extensive results reported in this report, and with Russian observations (Volkov et al. 1971). It is also what one would expect intuitively; namely, that in winter the ice is tightly held and cannot move rapidly, so that the water and Coriolis forces would be expected to be smaller than in the summer.

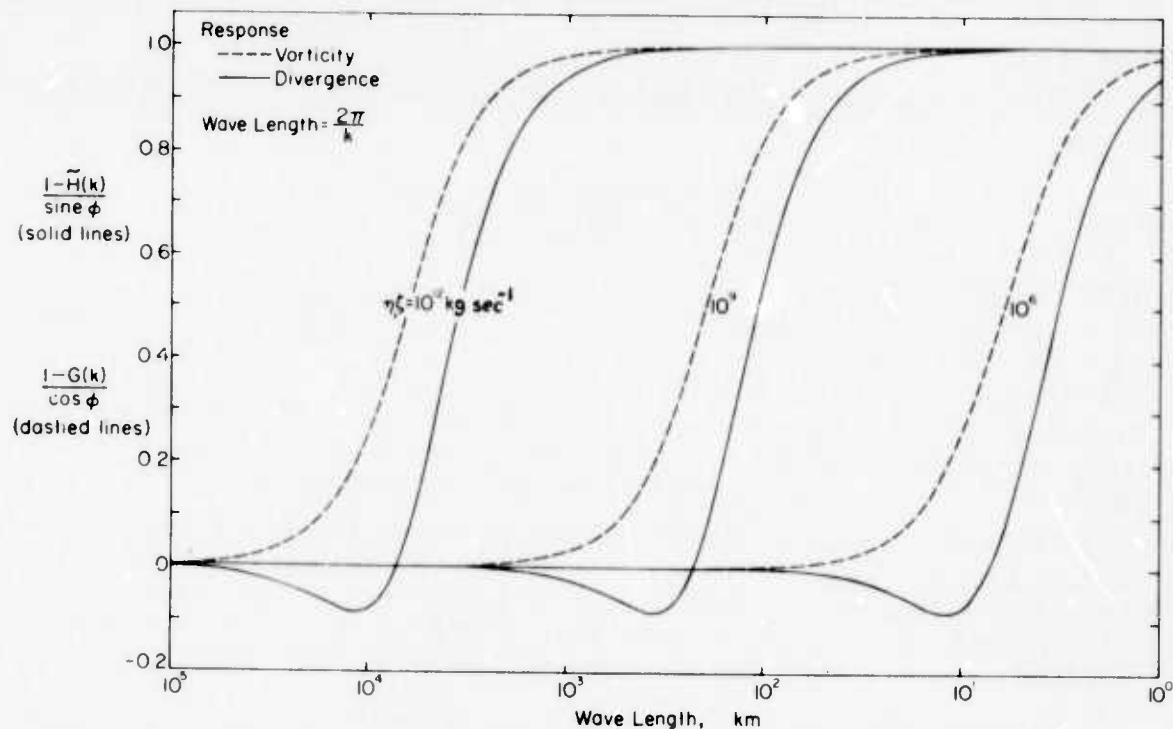


Figure 1. Wave number space response functions for the divergence rate and vorticity of the ice pack for different values of  $\eta$  and  $\zeta$ . The response functions operate on the atmospheric pressure field.

Finally, we note that if we used a series solution for the drift as given by Egorov (1970) it would be impossible to draw the above conclusions, because the series diverges for frequencies higher than the high pass cutoff frequency in  $1 - \bar{H}(k)$ .

#### General case – wavelength dependence

Clearly, it is critical what the "cutoff wavelengths" for  $1 - \bar{H}(k)$  and  $1 - \bar{G}(k)$  are. To illustrate typical forms of  $H(k)$  and  $G(k)$ , we use the following numerical values:

$$f = 1.46 \cdot 10^{-4} \text{ sec}^{-1}$$

$$m = 3.0 \cdot 10^3 \text{ kg m}^{-2}$$

$$\theta, \phi = 30^\circ$$

$$\rho = 1.3 \text{ kg m}^{-3}$$

$$K_a = 1.5 \cdot 10^1 \text{ m}^2 \text{ sec}^{-1}$$

$$K_w = 2.0 \cdot 10^{-2} \text{ m}^2 \text{ sec}^{-1}$$

$$B = 4.3 \cdot 10^{-2} \text{ kg sec}^{-1} \text{ m}^{-2}$$

$$D = 1.18 \text{ kg sec}^{-1} \text{ m}^{-2}.$$

The results for different values of  $\eta$  and  $\zeta$  are illustrated in Figure 1. For the  $\bar{H}(k)$  curve the key wavelength is the transition from positive to negative response. The results generally indicate

that for  $\eta, \zeta = 10^{12} \text{ kg sec}^{-1}$ , the "high wave number" pressure variations are those with wavelengths shorter than  $\sim 3000 \text{ km}$ . Since the synoptic scale for the Arctic is of the order of  $500 \text{ km}$  (Egorov 1971), the large  $\eta, \zeta$  limiting case is expected to be reasonably valid for  $\eta, \zeta = 10^{12} \text{ kg sec}^{-1}$ . For  $\eta, \zeta = 10^9 \text{ kg sec}^{-1}$ , on the other hand, the high wave number cutoff is such that one might expect the small  $\eta, \zeta$  case to be more applicable. This wavelength dependence explains why most calculations by Campbell (1965) and Campbell and Rasmussen (1973) have indicated diverging ice in a low pressure region. This is especially true of the yearly average drift where the mean yearly pressure field contains few high wave number spatial variations.

Figure 1 also illustrates the importance of the scale over which the pressure field is considered. For example, consider  $\eta$  and  $\zeta$  values such that the positive to negative transition in  $H(k)$  is at about  $1000 \text{ km}$ . Then, considering a high pressure system varying slowly in space with few high frequency components with wave numbers greater than  $1000 \text{ km}^{-1}$  the ice would be expected to converge. On the other hand, for a high pressure system varying very rapidly in space with significant variance at wave numbers greater than  $1000 \text{ km}^{-1}$ , the ice would be expected to diverge where the pressure was high. Clearly, it is very important to define the spatial scale used when speaking of diverging or converging ice.

### Comparison of Theory with Mesoscale Measurements

To determine how well the limiting forms of the predicted  $\Lambda$  and  $w$  values for large  $\eta$  and  $\zeta$  and infinite boundaries compare with mesoscale observations reported in Hibler et al. (1974), the local pressure at the main AIDJEX 1972 Camp (located at roughly  $75^\circ\text{N } 148^\circ\text{W}$ ), the measured ice divergence rate, and the measured ice vorticity were compared. The resulting time series are illustrated in Figure 2 with the dashed portions of the deformation rates representing data taken while the mesoscale array was only partially deployed. Calculation of the strain rate and vorticity time series is described in some detail in Part I of this report. In addition to these three time series, Figure 2 shows the calculated divergence of the wind velocity field and the fluctuations of the local atmospheric pressure from the average pressure over an approximately  $600\text{-km}$ -diameter region. The average pressure  $\bar{P}$  was estimated by taking the average of the camp pressure, four remote data buoy pressures located around the camp about  $300 \text{ km}$  away, and the Point Barrow pressure. For calculation of divergence of the wind velocity field, local wind speed and direction measurements at each of the three named stations were used. The distances and relative angles between the stations were taken as constant and estimated from position data for 19 March as reported by Thorndike et al. (1972). The basic computational equations are similar to those used in the strain calculations in Part I of this report. All of the time series shown in Figure 2 were smoothed with the same low pass filter having a transition band from  $0-3/80 \text{ cycles hr}^{-1}$  (Hibler 1972).

Correlation coefficients were calculated between all five of the time series (excluding the dashed portions of the divergence rate and vorticity) with the results listed in matrix form in Table 1. The standard error is based upon a number of degrees of freedom equal to the number of points correlated times the fraction of the spectrum passed by the filter.

As can be seen from Figure 2 and from the table of correlation coefficients, there is a positive correlation between the local pressure and the divergence rate and a negative correlation between pressure and vorticity as predicted by the large viscosity limiting case of the linear drift theory. The results also indicate that the spatial pressure fluctuation time series is quite similar to the camp pressure time series and has a similar correlation to the divergence rate and vorticity. This generally indicates that the pressure field has considerable variance at wavelengths shorter than  $600 \text{ km}$  and justifies to a limited extent the use of the infinite boundary solution for comparison.



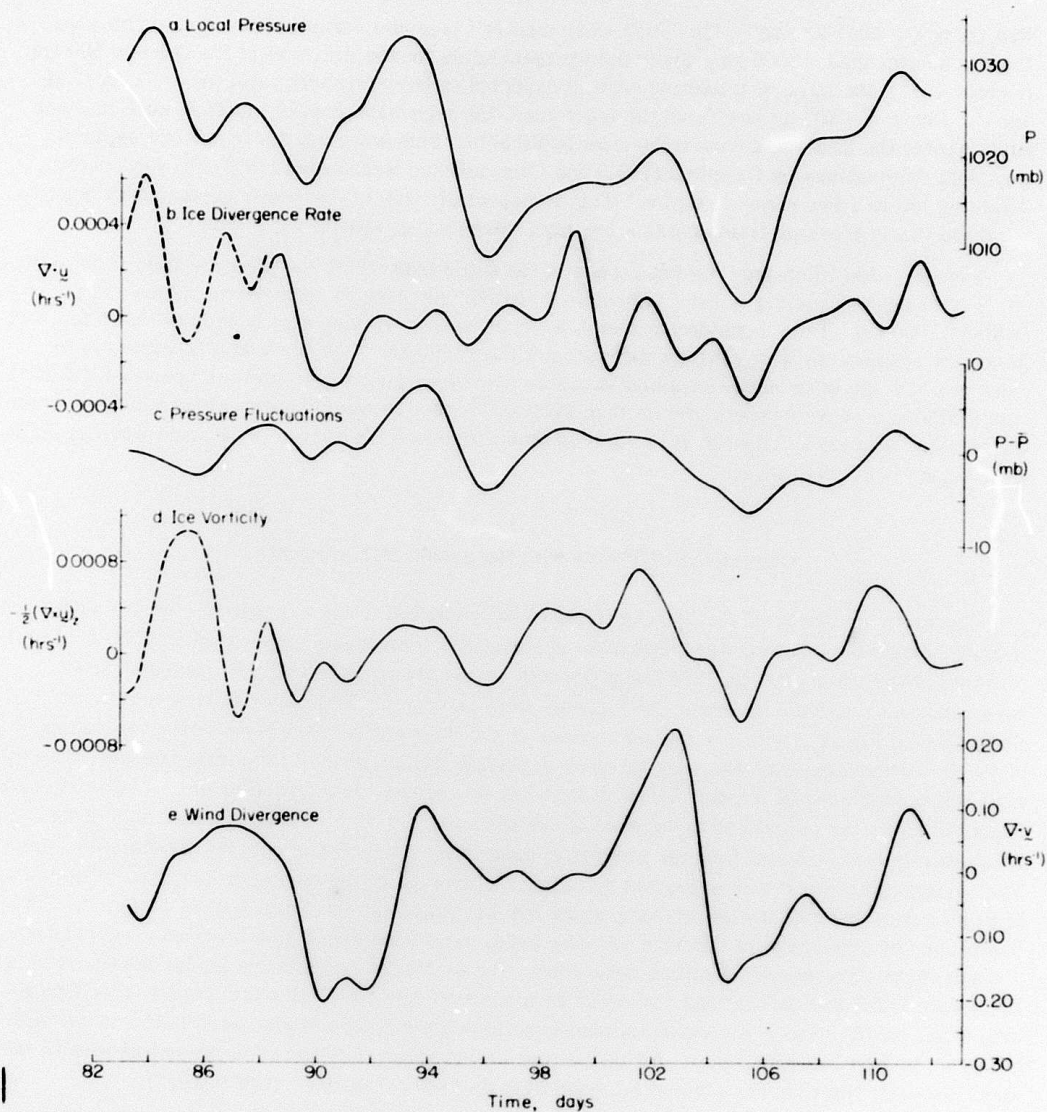


Figure 2. Comparison of experimental time series calculated from AIDJEX 1972 data. All curves were smoothed with a low pass filter having a transition band from 0 to  $3/80$  cycles  $\text{hr}^{-1}$ .

Table I. Correlation coefficient matrix between time series.  
 $u$  = ice velocity,  $v$  = wind velocity (standard error = 0.22).

	$\nabla \cdot u$	$\nabla \times u/2$	$P - \bar{P}$	$P$	$\nabla \cdot v$
$\nabla \cdot u$	1	-0.44	0.41	0.34	0.38
$\nabla \times u/2$	-0.44	1	-0.54	-0.46	-0.53
$P - \bar{P}$	0.41	-0.54	1	0.75	0.39
$P$	0.34	-0.46	0.75	1	0.21
$\nabla \cdot v$	0.38	-0.53	0.39	0.21	1

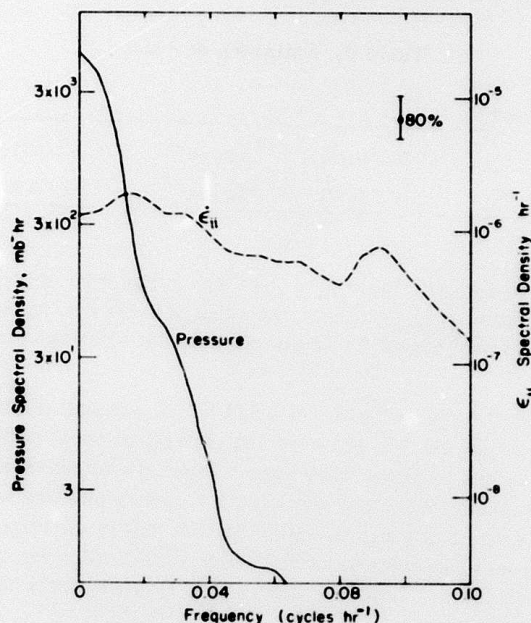


Figure 3. Spectra of atmospheric pressure and meso-scale ice divergence rate at the main AIDJEX 1972 camp.

The correlation between the vorticity and the divergence rate shows the expected negative value, with the magnitude of the vorticity being generally larger than that of the divergence rate. In particular, the ratio of the vorticity variance to the divergence rate variance is 3.8. The correlations between the wind divergence and the local pressure and pressure fluctuations are also positive, indicating the expected wind convergence in a low pressure region and vice versa in a high pressure region.

With respect to correlation at higher temporal frequencies, there are indications that there is little linear correlation between the pressure and the divergence rate at periods shorter than 24 hours. This is reasonable, since the atmospheric pressure variation is very nearly band limited. This is illustrated by the spectra of the pressure divergence rate ( $\dot{\epsilon}_{11}$ ) time series given in Figure 3. Clearly the pressure time series has comparatively little variance at periods shorter than 24 hours, which agrees with typical expected synoptic variation scales (Monin 1972, p. 9). The divergence rate spectrum, on the other hand, is relatively flat, although it does fall off by a factor of about 2 at 24-hour periods. These curves indicate that, although the meteorological driving forces on the ice are relatively smooth, the response of the ice is more complex and erratic in time probably due to random bumping of flows and opening and closing of leads.

#### Estimates of constitutive law parameters $\eta$ and $\zeta$

Assuming that the large viscosity limiting case of the linear drift theory is applicable to our observed mesoscale deformation, we may estimate the viscosity parameters  $\eta$  and  $\zeta$ . To do this we utilized the slopes of the regression lines of  $\Lambda$  and  $w$  upon  $P$  (using the curves in Figure 2), and also, for comparison, the regression lines of  $\Lambda$  and  $w$  upon  $P - \bar{P}$ . Equating these regression line slopes to the predicted slopes in eq 17 and 18 and inserting numerical values for  $B$ ,  $\phi$  and  $l$  (as previously listed), we obtained the results shown in Table II.



Table II. Estimates of  $\eta$  and  $\zeta$ .

Regression line used	$\eta$	$\eta + \zeta$
$\Lambda$ and $w$ upon $P$	$(1.70 \pm 0.73) \cdot 10^{12} \text{ kg sec}^{-1}$	$(5.3 \pm 3.34) \cdot 10^{12} \text{ kg sec}^{-1}$
$\Lambda$ and $w$ upon $P - \bar{P}$	$(0.66 \pm 0.23) \cdot 10^{12} \text{ kg sec}^{-1}$	$(1.94 \pm 0.95) \cdot 10^{12} \text{ kg sec}^{-1}$

According to the estimates in Table II,  $\eta$  and  $\zeta$  are of the order of  $10^{12} \text{ kg sec}^{-1}$  with  $\zeta$ , the bulk viscosity, being somewhat larger than  $\eta$ , the shear viscosity. This result agrees with intuitive expectations, since one would expect the ice to offer greater resistance to pure compression than to pure shear.

Table II also shows that the estimates of  $\eta$  and  $\zeta$  from different regression lines are quite similar. This illustrates that much of the observed correlation between the pressure field and the differential ice motion is due to higher wave number (spatial) variations in the pressure field. Such behavior suggests an explanation for why the infinite boundary solution works reasonably well since high wave number variations may be extracted by a real space response function that is well limited in space. Response functions to extract lower wave number variations, on the other hand, extend much further spatially and boundary effects would consequently be expected to be more critical at lower wave numbers.

Note also that reducing  $B$ , the wind stress constant, would reduce  $\eta$  and  $\zeta$ , and cause the response function to be more limited in space. Keeping this factor in mind, it is likely that our estimates of  $\eta$  and  $\zeta$  are only approximate and, in general, our deformation results could be commensurate with  $\eta$  and  $\zeta$  values varying anywhere from  $10^{11}$  to  $10^{12} \text{ kg sec}^{-1}$ .

Regarding the validity of the large viscosity limiting case, by referring back to Figure 1 we see that for values of  $\eta, \zeta \sim 10^{12}$  to  $10^{13} \text{ kg sec}^{-1}$  the wave number cutoff of the response functions lies in the range 1000 to 3000 km. These wavelengths are commensurate with or larger than expected synoptic variations in the pressure field, so that the use of the large  $\eta, \zeta$  limiting case appears to be justified for the data analyzed in this paper. However, for the smaller wavelengths in this range, the expected correlation would be primarily between the high wave number pressure components such as those estimated using  $P - \bar{P}$ . The large  $\eta, \zeta$  limiting case may also be justified for other boundary conditions (see App.).

It is interesting to note that compressive stresses predicted by our estimated values of  $\eta$  and  $\zeta$  are reasonable in terms of stresses predicted by Parmerter and Coon (1972). For example, maximum values of  $\Lambda$  are of the order of  $0.0004 \text{ hr}^{-1}$ , which yields for  $\zeta = 10^{12} \text{ g sec}^{-1}$  a compressive stress of  $1.1 \cdot 10^5 \text{ N m}^{-1}$  where we have used the Glen constitutive law. This is close to the  $0.1$  to  $0.4 \cdot 10^5 \text{ N m}^{-1}$  needed to cause ridging in 2-m ice by the bending-failure Parmerter and Coon ridge model. It is also similar to the maximum pressure difference of  $2 \cdot 10^5 \text{ N m}^{-1}$  obtained by Rothrock (1972) assuming the ice is incompressible.

Also of some interest is the numerical comparison of the calculated wind divergence rate with that estimated from the curvature of the pressure field. To do this we take as an estimate of the Laplacian  $-(4/5) [(P - \bar{P})/a^2]$  where  $a = 300 \text{ km}$ . Using the regression line of  $\nabla \cdot \mathbf{v}$  upon  $P - \bar{P}$ , we find an observed relation which yields an Ekman angle of  $44^\circ$ . Certainly these comparisons are only approximate, but they do indicate that the wind divergence estimated from the pressure field, using the geostrophic approximation and a constant Ekman angle, is the same order of magnitude as the calculated wind divergence rate.

### A More General Linear Constitutive Law

The previous sections generally indicate that most of the dominant aspects of the observed mesoscale drift behavior may be explained using a simple viscous ice rheology. It is useful to see if better agreement can be obtained using a linear viscoelastic law including memory effects. To do this we will carry out calculations using a more general constitutive law which allows the "viscosities" (bulk and shear) to vary with frequency and which can include both elastic and viscous behavior. One such law that is computationally similar to the Glen law is given by

$$\underline{F}(t) = \int_{-\infty}^t \eta(t-t') \nabla^2 u(t') dt' + \int_{-\infty}^t \zeta(t-t') \nabla [\nabla \cdot u(t')] dt' \quad (19)$$

where  $t$  denotes time.

Taking the temporal Fourier transform of this equation, we obtain (for convenience we simply replace  $t$  by  $\omega$  to denote temporal transforms)

$$\underline{F}(\omega) = \eta(\omega) \nabla^2 u(\omega) + \zeta(\omega) \nabla [\nabla \cdot u(\omega)] \quad (20)$$

where  $\eta(\omega)$  and  $\zeta(\omega)$  are analytic in the upper half plane to guarantee causality. Two particular limiting cases of this law are

1) Glen viscous law

$$\begin{aligned} \eta(t) &= \eta \delta(t) \\ \zeta(t) &= \zeta \delta(t) \end{aligned} \quad (21)$$

or, in frequency space

$$\begin{aligned} \eta(\omega) &= \eta \\ \zeta(\omega) &= \zeta \end{aligned} \quad (22)$$

where  $\eta$  and  $\zeta$  are constant viscosities.

2) Generalized Hooke's law

$$\begin{aligned} \eta(t) &= \eta \theta(t) \\ \zeta(t) &= \zeta \theta(t) \end{aligned} \quad (23)$$

where

$$\theta(t) = \begin{cases} 1 & t \geq 0 \\ 0 & t < 0 \end{cases} \quad (24)$$

or, in frequency space

$$\eta(\omega) = \frac{i}{\omega + i\delta} \eta$$

$$\zeta(\omega) = \frac{i}{\omega + i\delta} \zeta$$
(25)

with  $\delta$  infinitesimal.

Note that, for the Hooke's law case,  $\eta(\omega)$  and  $\zeta(\omega)$  both decrease with decreasing frequency and have a phase shift. The phase shift is the key indicator of elastic behavior.

#### Drift calculations using generalized law

It is clear that by using temporal transforms of all quantities the same formalism used for the simple viscous calculation may be used for the more generalized calculations. In particular, eq 6-11 may be formally extended to include the generalized constitutive law by replacing all quantities with temporal Fourier transforms; for example,  $\Lambda(\mathbf{x}) \rightarrow \Lambda(\mathbf{x}, \omega)$ ;  $\bar{\Lambda}(\mathbf{k}) \rightarrow \bar{\Lambda}(\mathbf{k}, \omega)$ . The arguments about limiting cases also are similar except that the magnitudes of  $\eta(\omega)$  and  $\zeta(\omega)$  are now the determining factors. In particular, for the large  $|\eta(\omega)|$ ,  $|\zeta(\omega)|$  limiting case, we have by analogy to eq 17 and 18 the results:

$$\lim_{|\eta(\omega)|, |\zeta(\omega)| \rightarrow \infty} \Lambda(\mathbf{x}, \omega) = \frac{B[P(\mathbf{x}, \omega) - \bar{P}] \sin \phi}{[\eta(\omega) + \zeta(\omega)]\rho f} \quad (26)$$

$$\lim_{|\eta(\omega)|, |\zeta(\omega)| \rightarrow \infty} w(\mathbf{x}, \omega) = \frac{-B[P(\mathbf{x}, \omega) - \bar{P}] \cos \phi}{2\eta(\omega)\rho f} \quad (27)$$

#### Comparison of general calculations with observations

To test eq 26 and 27, we need to determine the coherence (and phase lag) at different frequencies between the ice deformation time series and the atmospheric pressure time series. In particular, we would like to estimate  $\eta(\omega)$  and  $\zeta(\omega)$ . To carry out such an estimation, we note that for a linear system the frequency response function may be estimated by a cross spectral analysis (Jenkins and Watts 1968, p. 352). Using the unfiltered time series  $\Lambda(t)$ ,  $\omega(t)$  and  $P(t)$  (the camp atmospheric pressure), a cross spectral analysis was carried out using the lagged product method. Figure 4 shows the resulting coherence spectra and phase angles. The phase angle convention is such that a positive phase angle indicates a deformation signal lagging behind the atmospheric pressure. Using eq 26 and 27 as models, a negative phase angle of  $90^\circ$  would occur for a perfect Hooke's law behavior. Figure 5 illustrates the resulting amplitudes of  $\eta(\omega)$  and  $\zeta(\omega)$  obtained from estimates of the amplitude of the response functions of  $\Lambda$  and  $\omega$  upon  $P$ .

Figure 5 shows that both the bulk and shear "viscosities"  $\zeta(\omega)$  and  $\eta(\omega)$  exhibit a general decrease in amplitude with increasing frequency. Referring to Figure 4, the phase angle behavior does show some negative tendency indicative of elasticity, especially in the vorticity-pressure phase at higher frequencies. However, the overall behavior would generally seem to be more suggestive of a viscous behavior ( $0^\circ$  phase angle) rather than an elastic ( $-90^\circ$  phase angle) behavior.

The decrease in the "viscosity" amplitudes with increasing frequency is plausible on physical grounds; for example, let us imagine forcing a simultaneous sinusoidal oscillation in the divergence rate and shear rate of a given region of pack ice. The displacements of the oscillations will scale as  $1/\omega$ . Consequently, at very low frequencies the average compressive stress magnitude over one



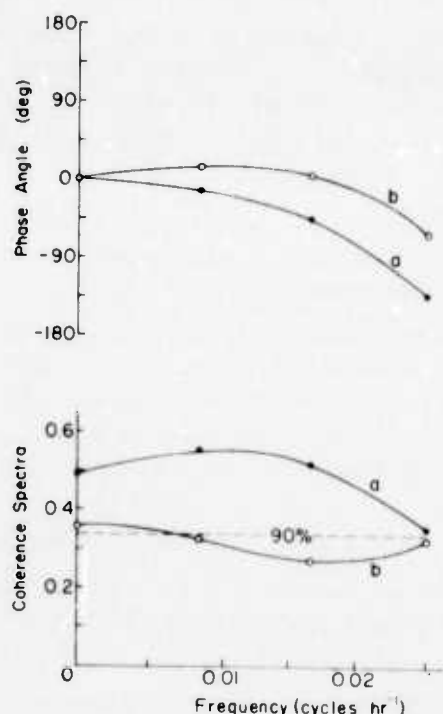


Figure 4. Coherence spectra and phase angles between a) vorticity and atmospheric pressure and b) divergence rate and atmospheric pressure. The 95% confidence limits for the phase angles vary from  $\pm 20^\circ$  to  $\pm 25^\circ$ .

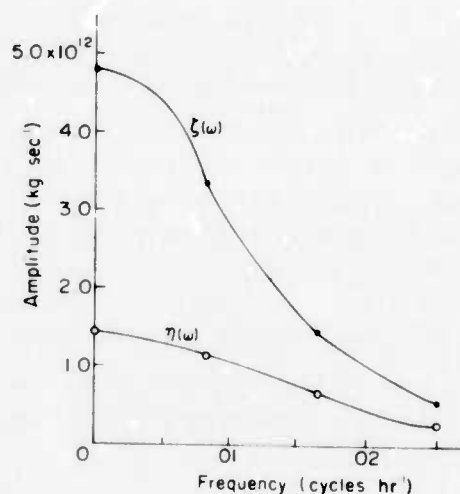


Figure 5. Frequency dependence of the generalized bulk and shear viscosity amplitudes. The amplitudes were obtained using the estimated response function of  $\Delta$  and  $w$  upon  $P$ .

cycle should be larger than that at higher frequencies because the larger compressive displacements might cause more thick ice to be crushed. Similarly, the shear stress should be larger for highly compressed ice; and since it is observed that shear and dilatation deformations generally occur simultaneously (Hibler et al. 1974), the average shear stress magnitude for a cycle might be expected to increase with the increasing displacement amplitude of the lower frequency cycles.

Referring back to Figure 3, we see that most of the atmospheric pressure variance is at wavelengths longer than 100 hours (90% of the pressure variance in Fig. 3 is at wavelengths greater than 120 hours). The fact that  $\zeta(\omega)$ , and especially  $\eta(\omega)$ , are relatively flat over these wavelengths (factor of  $\sim 3$  variation), coupled with the small phase shifts at low frequency, indicates that at low frequencies the Glen law limiting case [i.e.,  $\eta(\omega)$  and  $\zeta(\omega)$  constant] is a good first approximation to the generalized constitutive law. Since a linear law of any kind is probably only a crude approximation of the true ice rheology, the above results suggest that for predictive purposes there is little advantage in using a more generalized linear law as opposed to the Glen law.

### Conclusions

The most obvious inadequacies of the comparison made here are the neglect of finite boundaries in the drift predictions and the use of a simplified ice rheology. However, the calculations and comparisons in this paper do provide some helpful insight into expected differential sea ice drift for different ice conditions. Specifically, this study indicates several conclusions relative to AIDJEX.

1. The general agreement between the infinite boundary linear drift theory predictions and observations indicates that the dominant aspects of the mesoscale differential drift behavior observed in the 1971 and 1972 AIDJEX pilot programs may be explained using simple boundary conditions and straightforward linear constitutive laws. Certainly more complete calculations are needed to explain detailed drift behavior.

2. The solution of the linear drift calculation indicates the sensitive nature of differential comparisons in that smaller values of the constitutive law parameters  $\eta$  and  $\zeta$  do not only change the magnitude of the divergence rate but completely change its sign.

3. With respect to spatial scales, the infinite boundary linear drift solution indicates that for long wavelength variations in ice deformation the internal ice stress is unimportant, whereas for short wavelength variations the internal ice stress becomes critical. Consequently, ice drift calculations using the same viscous parameters may be quite different for pressure fields varying slowly in space as opposed to those varying rapidly. For example, given appropriate  $\eta$  and  $\zeta$  values, it is possible to have the ice converge in a high pressure system covering most of the Arctic Basin and to diverge in a high pressure system covering only a portion of the Arctic Basin.

Such spatial scaling effects may also have a bearing on comparisons of different time scales, since the temporal mean of the pressure field over, say a month, may vary more slowly in space than the mean daily pressure.

4. The cross spectral study of the atmosphere pressure and ice deformation in light of a generalized linear constitutive law indicates that our observed strain results may be better explained by a viscoelastic law including memory effects than by a simple viscous linear law. However, at low temporal frequencies ( $< 0.01 \text{ hr}^{-1}$ ) the generalized Hooke's law is similar to the Glen viscous law; this suggests that for general predictive purposes such a generalized linear law will probably yield only slight improvement over the Glen law.

5. Finally, the fact that differential drift follows the local pressure field reasonably well indicates that the ice velocity field may be quite nonlinear. Consequently, differential drift estimation using long strain lines ( $\sim 100 \text{ km}$ ) may not adequately resolve high wave number variations in the ice velocity field.

#### Literature Cited

- Campbell, W.J. (1965) The wind-driven circulation of ice and water in a polar ocean. *Journal of Geophysical Research*, vol. 70, no. 14, p. 3279-3301.
- Campbell, W.J. and L.A. Rasmussen (1973) A numerical model for sea ice dynamics incorporating three alternative ice constitutive laws. *Proceedings of the International Sea Ice Conference, Reykjavik, Iceland, May 1971*.
- Egorov, K.L. (1970) Theory of the drift of ice fields in a horizontally inhomogeneous wind field. *Problem Arktiki i Antarktiki*, no. 34, p. 71-77. English Translation in AIDJEX Bulletin no. 6, March 1971, p. 37-45.
- Egorov, K.L. (1971) Ice drift in an inhomogeneous pressure field. *Trudy, AANU*, vol. 303. English Translation in AIDJEX Bulletin no. 16, October 1972, p. 119-124.
- Glen, J.W. (1970) Thoughts on a viscous model for sea ice. *AIDJEX Bulletin*, no. 2, p. 18-27.
- Hibler, W.D. III (1972) Design and maximum error estimation for small error low pass filters. U.S. Army Cold Regions Research and Engineering Laboratory (USA CRREL) Research Report 304. AD 750116.

- Hibler, W.D. III, W.F. Weeks, S. Ackley, A. Kovacs and W.J. Campbell (1973) Mesoscale strain measurements of the Beaufort Sea pack ice (AIDJEX 1971). *Journal of Glaciology*, vol. 12, no. 65, p. 187-206.
- Hibler, W.D. III, W.F. Weeks, A. Kovacs and S. Ackley (1974) Differential sea ice drift, I: Spatial and temporal variations in sea ice deformation. *Journal of Glaciology*, vol. 13, no. 69, p. 437-455.
- Jenkins, G.M. and D.G. Watts (1969) *Spectral analysis and its applications*. San Francisco: Holden-Day.
- Monin, A.S. (1972) *Weather forecasting as a problem in physics*. Cambridge: MIT Press.
- Parmerter, R.R. and M.D. Coon (1972) Model of pressure ridge formation in sea ice. *Journal of Geophysical Research*, vol. 77, no. 33, p. 6565-6575.
- Reed, J.R. and W.J. Campbell (1962) The equilibrium drift of ice station alpha. *Journal of Geophysical Research*, vol. 67, no. 1, p. 281-297.
- Rothrock, D.A. (1972) Circulation of an incompressible ice cover. *AIDJEX Bulletin*, no. 18, p. 61-69.
- Skiles, F.L. (1968) Empirical wind drift of sea ice. In *Arctic drifting stations* (J.E. Sater, Editor). Arctic Institute of North America.
- Sutton, O.G. (1953) *Micrometeorology*. New York: McGraw-Hill.
- Thorndike, A., D. Bell, I. Viesnieks and A. Grill (1972) Station positions, azimuths, weather: 1972 AIDJEX pilot study: Preliminary data. *AIDJEX Bulletin*, no. 14, p. 63-71.
- Volkov, N.A., Z.M. Gudkovich and V.D. Uglev (1971) Results of the study of nonuniform ice drift in the Arctic Basin. *Trudy ANNI*, vol. 303. English Translation in AIDJEX Bulletin no. 16, October 1972, p. 82-96.
- Witting, J. (1972) Arctic ice circulation model (abstract). *Transactions, American Geophysical Union*, vol. 53, no. 11, p. 1016.

## APPENDIX. RELATIVE MAGNITUDES OF DIFFERENTIAL DRIFT FORCES

A substitution of measured drift parameters into eq 6 and 7 (of Part II of this report) allows a direct assessment to be made of the relative magnitudes of the wind, water and Coriolis stress terms independent of the value and functional form of the internal ice stress and independent of boundary conditions. Figure 2 shows that typical values for  $\Lambda$ ,  $w$  and  $\nabla \cdot \underline{v}$  wind are given by  $\Lambda \sim 0.0002 \text{ hr}^{-1}$ ,  $w \sim 0.0006 \text{ hr}^{-1}$ ,  $\nabla \cdot \underline{v} \sim 0.14 \text{ hr}^{-1}$ . Using eq 6 and values of  $B$ ,  $D$ ,  $\theta$ ,  $\phi$  and  $f$  as mentioned earlier, we find that the wind stress term is about 10 to 20 times as large as the water and Coriolis stress terms. This indicates that for differential drift the neglect of water strain and Coriolis terms for compact conditions is reasonable, and thus justifies the use of the large  $\eta, \zeta$  drift solution.

It is useful to contrast the differential drift results in this paper with regular drift results. For regular (nondifferential) drift, the wind to ice velocity ratio is typically of the order of 50 or less (Reed and Campbell 1962, Skiles 1968). Thus, since  $D/B \sim 50$ , for regular drift, water and Coriolis stress terms may not be neglected. For differential drift results in this paper, on the other hand, the ratio of wind divergence to ice divergence or vorticity is  $\sim 300$ , so that water and Coriolis stress are relatively small.